

# Effects of Water Vapour on Oxidation

### 11.1 INTRODUCTION

In 1988, Kofstad [1] wrote, ‘It is well known that most technical steels oxidise faster in water vapour or in air or combustion gases containing water vapour than in dry oxygen. The reasons for this are poorly understood’. At a subsequent workshop on high-temperature corrosion [2], it was concluded that understanding remained incomplete. Since then, considerable experimental effort has led to a better definition of the problem and an improved level of understanding. Recent reviews [3–5] describe much of this work and make clear that apparent conflicts persist, and there is still much to learn as to underlying mechanisms in some cases.

The potential severity of the problem is illustrated in Fig. 11.1, where the results of oxidising a ferritic 9% Cr steel at 650°C in  $\text{N}_2\text{-O}_2$  and  $\text{N}_2\text{-O}_2\text{-H}_2\text{O}$  are compared. The dry gas produced an extremely thin ( $\sim 50$  nm) scale with a chromium-rich layer adjacent to the alloy, and protective behaviour was achieved. This was not the case in wet gas, where a porous, multiphase scale grew rapidly. The mechanisms whereby water vapour changes the phase constitution, microstructure and growth rate of the oxidation product are of both fundamental interest and practical importance.

Water vapour is present in many gases of industrial importance. Atmospheric air contains water vapour at levels which vary with temperature and relative humidity. A temperature range of 18–28°C corresponds to saturation values (ie, at 100% relative humidity) of  $p_{\text{H}_2\text{O}} = 0.02\text{--}0.04$  atm. As will be seen later, these levels are sufficient to affect the oxidation rates of many alloys. Thus the results of laboratory experiments using uncontrolled atmospheric air are subject to these affects. Conversely, oxidation rates to be expected in, for example, air preheaters cannot be predicted from laboratory data obtained using dry air.

Water vapour is invariably a constituent of combustion gases and can therefore affect corrosion in engines, direct-fired furnaces and recuperators. It is also present in synthesis gas and coal gas, along with hydrogen. Similar mixtures are generated in fuel cell anode gas streams. Finally, pure steam is the

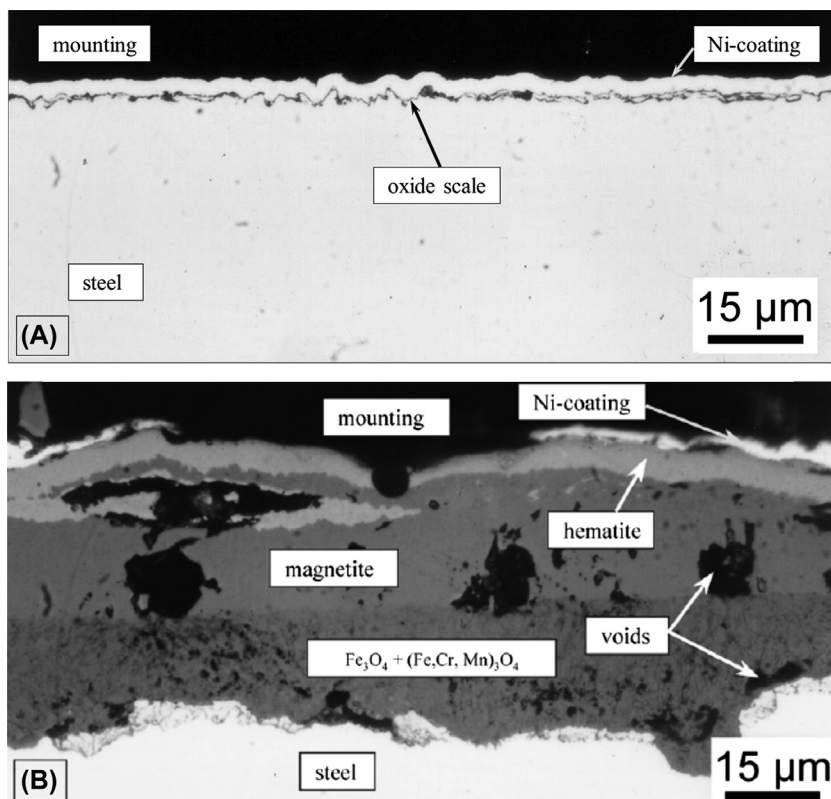


**FIGURE 11.1** Cross-section of P91 steel after 100 h exposure at 650°C to (A)  $\text{N}_2$ -1% $\text{O}_2$  and (B)  $\text{N}_2$ -1% $\text{O}_2$ -2% $\text{H}_2\text{O}$ . Reprinted from J. Ehlers, D.J. Young, E.J. Smaardijk, A.K. Tyagi, H.J. Penkalla, L. Singheiser, W.J. Quadakkers, *Corros. Sci.* 48 (2006) 3428, with permission from Elsevier.

working fluid in many power generating systems and is handled as a process stream in a diversity of chemical plants.

The water molecule is very stable with respect to its dissociation



as reflected by the free energy change

$$\Delta G_1^\circ = 246,440 - 54.8 T \text{ J mol}^{-1} \quad [11.2]$$

Consequently, the value of  $p_{\text{O}_2}$  in gases containing free molecular oxygen is essentially unchanged by reaction [11.1] if water vapour is added. In pure steam or inert gas-water vapour mixtures, the equilibrium value of  $p_{\text{O}_2}$  is determined by the extent of  $\text{H}_2\text{O}$  dissociation. In the case of pure steam, the dissociation of 1 mol yields  $x$  moles of  $\text{H}_2$  and  $x/2$  moles of  $\text{O}_2$ , with  $x$  to be

calculated from the equilibrium expression. Using the method of Section 2.1, we find

$$K_1^2 = \frac{x^3}{2(1-x)^2(1+x/2)} P_T \quad [11.3]$$

where  $P_T$  is the total pressure. Because  $K_1$  is small,  $x \ll 1$  and [11.3] is well approximated by

$$x = \left( \frac{2K_1^2}{P_T} \right)^{\frac{1}{3}} \quad [11.4]$$

$$p_{O_2} = xP_T \quad [11.5]$$

Equilibrium oxygen partial pressures calculated in this way are seen in Fig. 11.2 to be high enough to form  $Fe_2O_3$  on iron at low temperatures. As expected,  $p_{O_2}$  increases with temperature and total pressure. At high temperatures, hematite formation in steam is not possible, unless the pressure is large.

If impurity amounts of  $O_2$  are present in the steam, then  $p_{O_2}$  would be set by the impurity level rather than  $H_2O$  dissociation. However, it seems likely that any such impurities would be quickly scavenged by a reaction with oxidising metal, and the water dissociation equilibrium thereby restored.

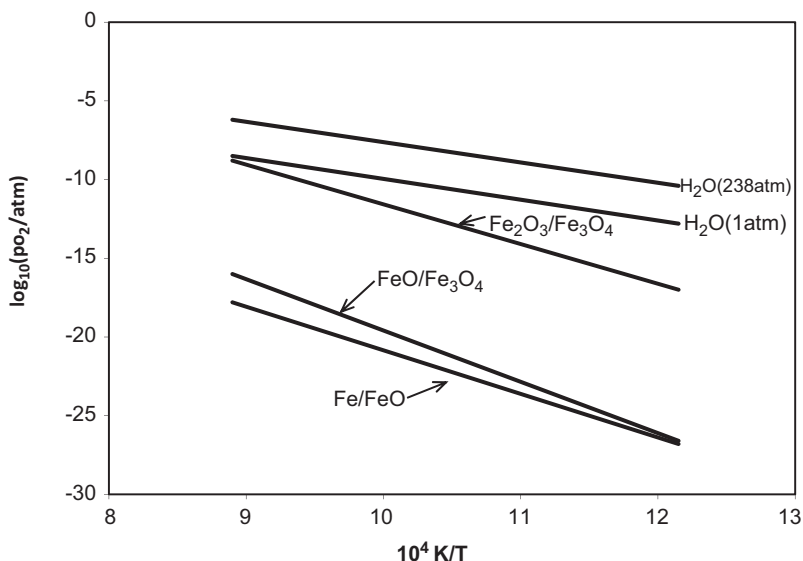


**FIGURE 11.2** Equilibrium oxygen partial pressures calculated for pure steam at indicated pressures compared with values required for oxide formation.

A final factor to be recognised in considering the reacting gas phase is hydrogen generation. In the case of pure steam, the oxidation process

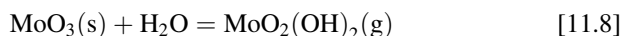
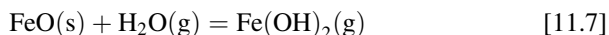


produces hydrogen. Depending on mass transfer rates between the scale surface and steam phases, the local situation could be similar to that reached in synthesis gas or a laboratory  $H_2/H_2O$  mix. In the presence of free molecular oxygen, however, any hydrogen generated in this way is presumably oxidised rapidly to water vapour.

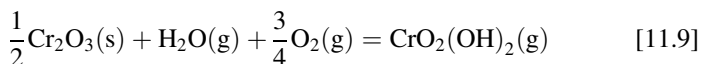
Water vapour can, in principle, interact with an oxidising metal in a number of ways. It can participate in surface reactions, thereby modifying the scale-gas interface or even producing volatile hydrated species. It can interact with the scale interior, affecting its microstructure and properties, including its transport behaviour. These interactions include the possible dissolution of hydrogen in the oxide and the generation of lattice point defects. Finally, hydrogen generated by reaction [11.6] can dissolve in the metal itself.

## 11.2 VOLATILE METAL HYDROXIDE FORMATION

Several metal oxides form volatile compounds by direct reaction with water vapour. Hydroxides and oxyhydroxides can be produced by hydration, eg,



In addition, simultaneous oxidation and hydration sometimes occurs, eg,



Thermodynamic data for the more important reactions are summarised in Table 11.1, and a more extensive collection has been provided by Jacobson et al. [14].

Volatilisation of a protective scale leads to accelerated consumption of the scale-forming element and its depletion in an alloy. In the usual case of an alloy exposed to a flowing gas, the rate at which a vapour species produced at low concentration at the oxide-gas interface transfers into the bulk of the gas is described by [2.157] and [2.158]. Assuming that none of the hydroxide is initially present in the gas, these two equations are combined to yield an expression for the molar flux

$$J_i = \frac{0.664}{RT} \left( \frac{D_{AB}^4}{v_g} \right)^{\frac{1}{6}} \left( \frac{v}{L} \right)^{\frac{1}{2}} p_i \quad [11.10]$$

Here  $p_i$  is the hydroxide partial pressure at the scale surface, which is calculated on the supposition of scale-gas equilibrium. In order to assess the

TABLE 11.1 Free Energies of Metal Hydroxide Formation Reactions<sup>a</sup>

Reaction	$\Delta G^\circ = A + BT$ (J)		References
	A	B	
$\text{FeO(s)} + \text{H}_2\text{O(g)} = \text{Fe(OH)}_2\text{(g)}$	175,700	−31.4	[7]
$\text{Fe}_3\text{O}_4\text{(s)} + 3\text{H}_2\text{O(g)} = 3\text{Fe(OH)}_2\text{(g)} + \frac{1}{2}\text{O}_2\text{(g)}$	818,400	−193	[8]
$\text{Fe}_2\text{O}_3\text{(s)} + 2\text{H}_2\text{O(g)} = 2\text{Fe(OH)}_2\text{(g)} + \frac{1}{2}\text{O}_2\text{(g)}$	663,300	−200	[9]
$\text{NiO(s)} + \text{H}_2\text{O(g)} = \text{Ni(OH)}_2\text{(g)}$	219,000	−50.7	[8]
$\text{Cr}_2\text{O}_3\text{(s)} + 2\text{H}_2\text{O(g)} + \frac{3}{2}\text{O}_2\text{(g)} = 2\text{CrO}_2\text{(OH)}_2\text{(g)}$	53,500	45.5	[10]
$\text{Al}_2\text{O}_3\text{(s)} + 3\text{H}_2\text{O(g)} = 2\text{Al(OH)}_3\text{(g)}$	220,000	−14.7	[11]
$\text{SiO}_2\text{(s)} + 2\text{H}_2\text{O(g)} = \text{Si(OH)}_4\text{(g)}$	47,900	72.3	[12–14]

<sup>a</sup>For mole numbers of reactions as written

suitability of metal oxides for exposure to water vapour, it is necessary to establish at what temperatures the values of  $p_i$  become high enough for volatilisation to be significant.

11.2.1 Chromia Volatilisation

The presence of water vapour has long been known [1,15–17] to accelerate the degradation of chromia-forming alloys. It has been discovered that water vapour has adverse effects on such alloys at relatively low temperatures [18–20]. Asteman et al. [18,21] investigated the reaction between O<sub>2</sub>-H<sub>2</sub>O gas mixtures and the Cr<sub>2</sub>O<sub>3</sub> scale grown on 304L (Fe-18Cr-8Ni) stainless steel at 600°C. They showed that weight gain kinetics were accelerated by increasing  $p_{\text{H}_2\text{O}}$  and the gas flow velocity. The faster oxidation was attributed to lower Cr/Fe ratios in the scales, and consequently more rapid diffusion. The change in Cr/Fe ratio was due to chromium volatilisation, detected by analysing deposits condensed from the reaction gas downstream from the oxidised stainless steel.

As seen in Fig. 11.3, the Cr-O-H system contains a diversity of volatile species. Ebbinghaus [22] has reviewed the early thermodynamic data for this system. Using those data together with more recent results of Opila et al. [10] for CrO<sub>2</sub>(OH)<sub>2</sub>, the equilibrium partial pressures shown in Fig. 11.3 were calculated for humid air ( $p_{\text{O}_2} = 0.21$  atm,  $p_{\text{H}_2\text{O}} = 0.04$  atm). It is clear that CrO<sub>2</sub>(OH)<sub>2</sub> is the predominant vapour species at temperatures below about 1000°C. The rate at which this species evaporates into a flowing gas stream is now calculated.

The reaction gas modelled here is air +10% H<sub>2</sub>O, an approximation to the water vapour content of a combustion gas. Calculation of the diffusion coefficient is performed using the Chapman–Enskog description [23] of the

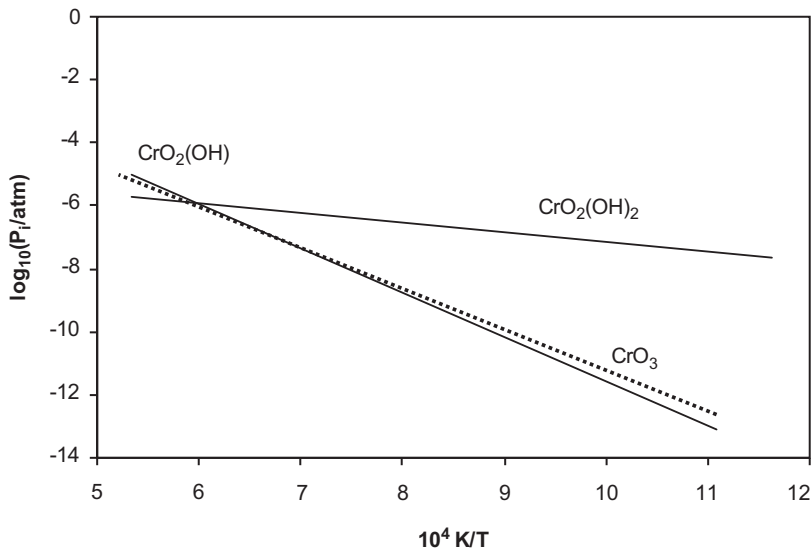


**FIGURE 11.3** Temperature dependence of selected Cr-O-H species vapour pressures calculated for  $p_{\text{O}_2} = 0.21$  atm and  $p_{\text{H}_2\text{O}} = 0.04$  atm using thermodynamic data from Ebbinghaus [22] and Opila et al [10]. Data from B.B. Ebbinghaus, *Combust. Flame* 93 (1993) 119; E.J. Opila, D.L. Myers, N.S. Jacobson, I.M.D. Nielson, D.F. Johnson, J.K. Olminky, M.D. Allendorf, *J. Phys. Chem. A* 111 (2007) 1971.

kinetic theory of gases, based on a simplified model of the gas as a binary  $\text{N}_2\text{-CrO}_2(\text{OH})_2$  mixture. Mass transfer parameters calculated [24] for  $P_T = 1$  atm are shown in Table 11.2. The part of the mass transfer coefficient,  $k_m$ , which depends only on the gas state functions  $T$ ,  $P$ ,  $X_i$  is seen to be relatively insensitive to temperature. The remaining term  $(\nu/L)^{1/2}$  varies with experimental design. Oxidation results discussed here were obtained by Pint [25,26], using specimens of length  $L = 18$  mm, and an inlet (room temperature and pressure) volumetric flow rate of 0.85 L/min, corresponding to  $\nu = 17$ , 18 and 20 mm/s at 650, 700 and 800°C, respectively. These values lead to the mass transfer coefficients shown in Table 11.3. Values of  $p_{\text{CrO}_2(\text{OH})_2}$  for chromia in

TABLE 11.2 Mass Transfer Parameters for $\text{CrO}_2(\text{OH})_2$ in Air-10% $\text{H}_2\text{O}$ [24]			
$T$ (°C)	$D_{\text{AB}}$ ( $\text{cm}^2 \text{s}^{-1}$ )	$\nu$ ( $\text{cm}^2 \text{s}^{-1}$ )	$0.664(D_{\text{AB}}^4/\nu)^{1/6}$ ( $\text{cm s}^{-1/2}$ )
650	$0.8 \pm 0.1$	1.077	$0.56 \pm 0.04$
700	$0.9 \pm 0.1$	1.169	$0.60 \pm 0.05$
800	$1.0 \pm 0.1$	1.380	$0.63 \pm 0.08$

TABLE 11.3 Chromium Loss<sup>a</sup> as CrO<sub>2</sub>(OH)<sub>2</sub> in Air –10% H<sub>2</sub>O

<i>T</i> (°C)	<i>k<sub>m</sub></i> (cm s <sup>−1</sup> )	<i>p</i> <sub>CrO<sub>2</sub>(OH)<sub>2</sub></sub> (atm)	<i>J</i> <sub>Cr</sub> (g cm <sup>−2</sup> s <sup>−1</sup> )
650	0.54 ± 0.04	8.4 × 10 <sup>−8</sup>	(3.1 ± 0.2) × 10 <sup>−11</sup>
700	0.60 ± 0.05	1.6 × 10 <sup>−7</sup>	(6.3 ± 0.5) × 10 <sup>−11</sup>
800	0.66 ± 0.08	3.0 × 10 <sup>−7</sup>	(1.2 ± 0.1) × 10 <sup>−10</sup>

<sup>a</sup>Expressed as mass of metal.

equilibrium with air +10%H<sub>2</sub>O calculated from the reaction free energy for [11.9] are also shown in the table, along with the resulting chromium loss rates predicted from [11.10]. The value of these predictions is now assessed by performing a chromium mass balance for oxidised alloy foil.

Foil specimens (ca. 100 μm thickness) of alloy 709 (Fe-25Ni-20Cr base) oxidised in air – 10% H<sub>2</sub>O for up to 10<sup>4</sup> h at 650, 700 and 800°C [25,26] grew scales of chromia containing low levels of iron and manganese. After lengthy exposures, large iron-rich nodules formed as the surface became depleted in chromium, and the reaction rate accelerated. Electron microprobe analysis of the entire thickness of reacted samples provided measurement of the residual chromium content. The amounts of chromium in the scales were calculated from their thicknesses, assuming that the oxide was pure Cr<sub>2</sub>O<sub>3</sub>. The sum of the amounts of chromium in the remaining foil and its scale was compared with the amount originally present in unreacted foil, and the deficit noted as a function of time. These values are compared in Fig. 11.4 with chromium vapourisation losses

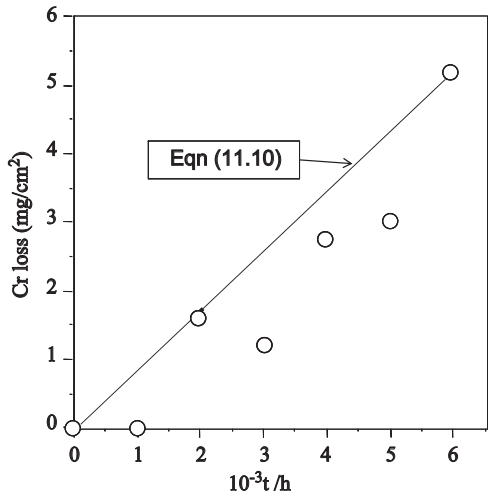
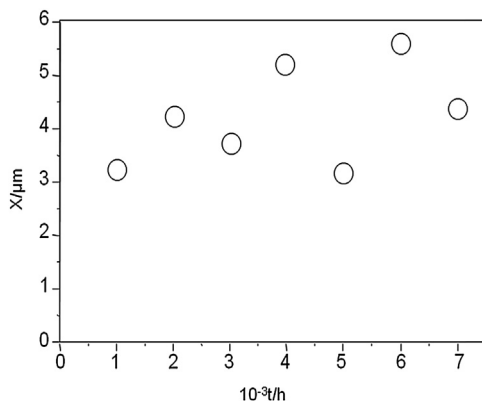


FIGURE 11.4 Comparison of measured chromium losses with values calculated for evaporation loss from alloy 709 exposed at 800°C to air +10% water vapour. Data from D.J. Young, B.A. Pint, *Oxid. Met.* 66 (2006) 137.



**FIGURE 11.5** Scale thickening kinetics for alloy 709 exposed at 800°C to air +10% H<sub>2</sub>O(g). Data from D.J. Young, B.A. Pint, *Oxid. Met.* 66 (2006) 137.

calculated from the flux value given in Table 11.3. The good agreement shows that the observed chromium depletion can be completely accounted for by Cr<sub>2</sub>O<sub>3</sub> scale formation and CrO<sub>2</sub>(OH)<sub>2</sub> evaporation.

Vaporisation losses can also be investigated by considering scale-thickening kinetics. The thickness increases as a result of solid-state diffusion and decreases by evaporation, leading [27] to the rate Eq. [1.36]. Thus  $X$  increases to a steady-state value,  $X_{ss}$ , where  $dX/dt = 0$ , and

$$X_{ss} = \frac{k_p}{k_v} \quad [11.11]$$

Scale thicknesses measured from polished cross-sections of oxidised alloy 709 are shown in Fig. 11.5. Although scatter is considerable, the data appear to conform with Eq. [1.36], with  $X_{ss} = 5 \pm 1 \mu\text{m}$  at 800°C. Evaluating  $k_p$  as  $(2.0 \pm 0.1) \times 10^{-14} \text{ cm}^2 \text{ s}^{-1}$  from early stage kinetics [24], it is found from [11.11] that  $k_v = (4 \pm 1) \times 10^{-11} \text{ cm s}^{-1}$ , corresponding to an average evaporative flux of chromium,  $J_{Cr} = (1.4 \pm 0.3) \times 10^{-10} \text{ g cm}^{-2} \text{ s}^{-1}$ . This value is in good agreement with the mass transfer calculation result (Table 11.3) of  $J_{Cr} = (1.2 \pm 0.1) \times 10^{-10} \text{ g cm}^{-2} \text{ s}^{-1}$ .

Calculations based on Eq. [11.10] and applied to the common laboratory situation of relatively slow gas flow rates in tubular reactors are subject to error because the boundary layer thickness may not be small compared to the tube cross-section. Fortunately, the errors are frequently small, as discussed in Section 11.2.5.

### 11.2.2 Chromia Volatilisation in Steam

The performance of chromia scales in pure steam environments is relevant to service conditions in supercritical and ultrasupercritical steam power plants.



The oxygen potential in high purity steam is controlled by reaction [11.1], and therefore  $p_{\text{O}_2}$  is given by [11.4] and [11.5]. The value of  $p_{\text{CrO}_2(\text{OH})_2}$  is then found from the equilibrium expression for [11.9]

$$K_9 = \frac{p_{\text{CrO}_2(\text{OH})_2}}{p_{\text{O}_2}^{\frac{3}{2}} p_{\text{H}_2\text{O}}} \quad [11.12]$$

setting  $p_{\text{H}_2\text{O}} = P$ , leading to the result

$$p_{\text{CrO}_2(\text{OH})_2} = K_9 \left( \frac{K_{12}}{2} \right)^{\frac{1}{2}} P^{\frac{3}{2}} \quad [11.13]$$

which is seen to be strongly pressure-dependent.

Conventional boilers operate at maximum steam pressure of 120–150 atm in their superheaters. Supercritical boilers have superheater pressures of  $\sim 240$  atm. Equilibrium partial pressures for  $\text{CrO}_2(\text{OH})_2$  calculated for these conditions from [11.13] are shown in Fig. 11.6. The values are low as a result of the very low oxygen partial pressures in pure steam. Only at high total pressure does the  $\text{CrO}_2(\text{OH})_2$  partial pressure become significant. Calculation [24] of chromium volatilisation rates shows that they are very low, except at very high pressures. The calculation is, however, based on the Chapman–Enskog description, which depends on the assumption of ideal gas behaviour. It will not apply to the supercritical regime, and no prediction for chromia volatilisation can be made on this basis.

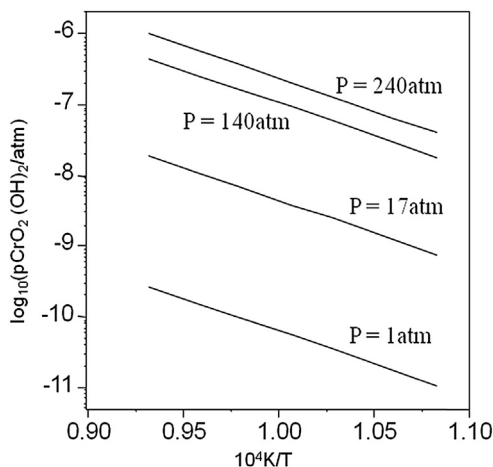


FIGURE 11.6 Equilibrium  $\text{CrO}_2(\text{OH})_2$  partial pressures calculated for pure steam.

### 11.2.3 Effects of Chromia Volatilisation

Increasing water vapour partial pressures are predicted from the preceding analysis to accelerate the rate of chromia volatilisation for a given value of  $p_{O_2}$ . In the case of  $O_2 + H_2O$  gas mixtures

$$P_T = p_{O_2} + p_{H_2O} \quad [11.14]$$

and, at  $P_T = 1$  atm, it follows from [11.12] that

$$p_{CrO_2(OH)_2} = K_9(1 - p_{H_2O})^{\frac{3}{4}}p_{H_2O} \quad [11.15]$$

The maximum value of  $p_{CrO_2(OH)_2}$  is found by setting the differential  $dp_{CrO_2(OH)_2}/dp_{H_2O} = 0$ , whereupon it is found that

$$(1 - p_{H_2O}) = \frac{3}{4}p_{H_2O} \quad [11.16]$$

which has the solution  $p_{H_2O} = 0.57$  atm. Thus the volatilisation rate is predicted to increase with  $p_{H_2O}$  up to a maximum at this value.

Data to test this prediction are available only at low water vapour pressures. Jianian et al. [28] showed that the oxidation kinetics of binary Fe-Cr alloys in  $O_2$ - $H_2O$  atmospheres ( $P_T = 1$  atm,  $p_{H_2O}$  up to 0.25 atm) were initially protective, before entering a breakaway stage. The time taken to reach breakaway decreased with increasing  $p_{H_2O}$  (Fig. 11.7) and increased with increasing alloy

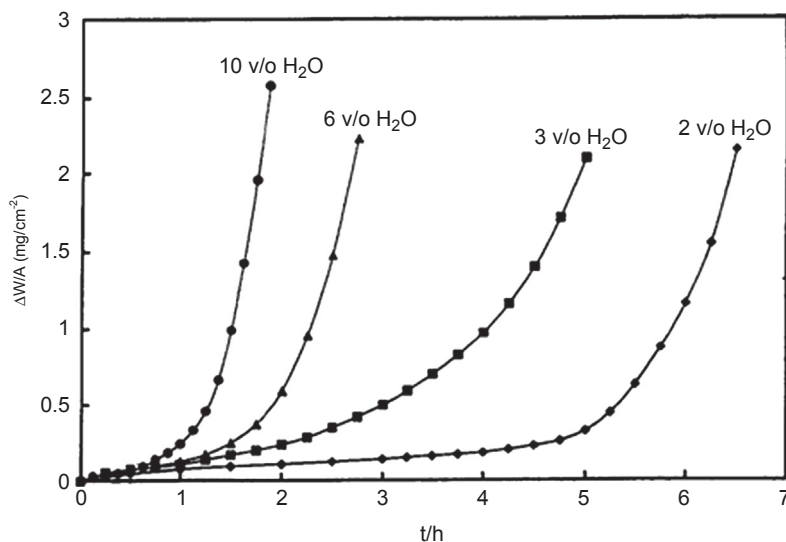


FIGURE 11.7 Oxidation kinetics for Fe-15Cr in  $O_2$ - $H_2O$  mixtures at  $900^\circ\text{C}$ . With kind permission from S. Jianian, Z. Longjiang, L. Tiefan, *Oxid. Met.* 48 (1997) 347, Springer Science and Business Media.

chromium level. In agreement with earlier results [29–32], breakaway was found to be associated with the progressive spread of iron-rich nodules until the previously protective  $\text{Cr}_2\text{O}_3$  scale was destroyed and replaced with a porous, multilayered iron-rich scale. This behaviour is consistent with chromium depletion via volatilisation, leading to iron enrichment in the scale. The rate of depletion increases with  $p_{\text{H}_2\text{O}}$ , as discussed above. However, the time taken to reach a critical depletion level depends also on the size of the chromium reservoir available in the original alloy. The rate at which the initial chromia scale grows,  $k_p$ , also varies with  $p_{\text{H}_2\text{O}}$ . This affect is discussed in Section 11.4.

There are situations where the rate of chromium volatilisation is insignificant from the point of view of material durability, but unacceptable as a source of contamination. Consider semiconductor processing, where atmospheric pressure chemical vapour deposition (APCVD) can be used to deposit doped and undoped  $\text{SiO}_2$  onto silicon wafers at temperatures of about 400–600°C. Acceptable impurity metal deposition levels are very low, at about  $10^{10}$  atom  $\text{cm}^{-2}$ . For this reason, ceramic hardware is often preferred, although alloys would offer practical advantages. Bailey [33] demonstrated that the chromia-forming IN601 (Ni-22Cr-17Fe-1.7Al) exposed to APCVD conditions evaporated  $\text{CrO}_2(\text{OH})_2$  at rates which exceeded acceptable limits for processed wafers. An alumina-forming alloy was found to provide satisfactory performance.

Solid oxide fuel cells provide another example of chromium contamination at their operating temperatures of 750–900°C. A schematic view of a cell is shown in Fig. 11.8. Zirconia is used as an oxygen ion electrolyte between a cathode exposed to air and an anode exposed to the fuel gas. The porous electrodes are electronically conducting perovskites,  $(\text{La,Cr})\text{MO}_3$ , where M is Co, Mn or Cr. These cells are stacked together to obtain usable power outputs. In the design depicted, the cells are planar and are separated by plates which provide structural support, electrical connection and gas stream separation. A practical materials solution is a chromia-forming alloy [34], because the resulting oxide scale has fairly good electronic conductivity. Unfortunately, however, it evaporates  $\text{CrO}_2(\text{OH})_2$  in humid air.

Das et al. [35] and Quadackers et al. [36] have demonstrated that exposure to air of normal humidity at 900–950°C leads to chromium transport from the chromia scale throughout the porous perovskite cathode. Reaction between the gaseous chromium species and the perovskite produces phases such as  $\text{MnCr}_2\text{O}_4$ , which increase the electrical resistivity of the cathode to an unacceptable level.

### 11.2.4 Silica Volatilisation

The behaviour of silica in combustion environments is an important issue, because the silicon-based ceramic composites (SiC, etc.) are protected at high temperatures by a slow-growing silica scale. The principal volatile species

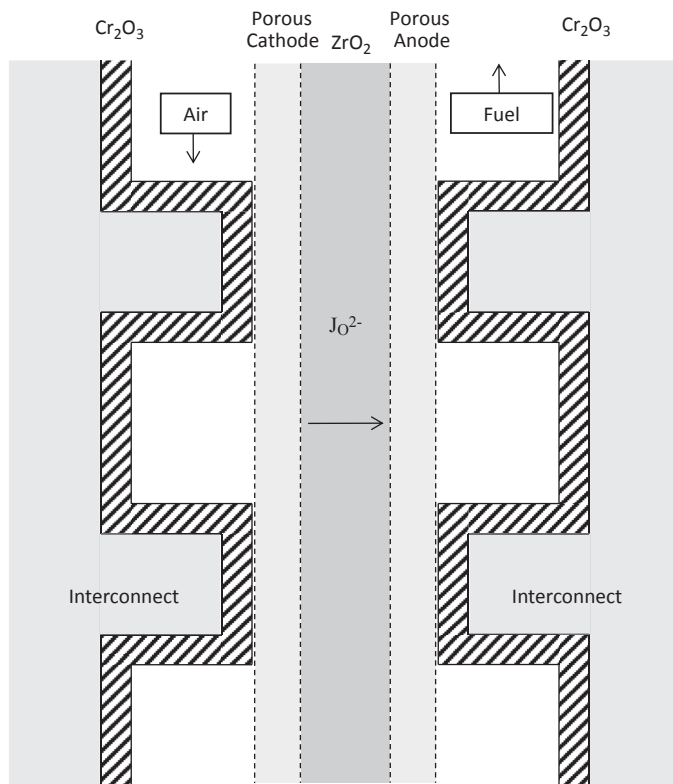
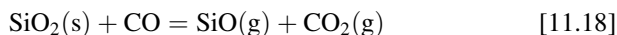
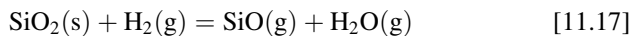


**FIGURE 11.8** Schematic section of solid oxide fuel cell with chromia-forming alloy interconnect plates.

formed by interaction between silica and water vapour at temperatures around 1200°C is  $\text{Si}(\text{OH})_4$ , but at temperatures above 1400°C, it is  $\text{SiO}(\text{OH})_2$  [12–14]. Under strongly reducing conditions, on the other hand, the principal gas species is SiO, formed by the reactions [37,38]



Thus volatilisation is possible in a wide range of gas atmospheres.

Opila and Hann [39] showed that oxidation of SiC in flowing  $\text{H}_2\text{O}/\text{H}_2$  gas mixtures led to weight uptake followed by weight loss (Fig. 11.9). The kinetic data were analysed using the integrated form [27] of [1.36]:

$$\int \frac{X}{k_p - k_v X} dX = t \quad [11.19]$$

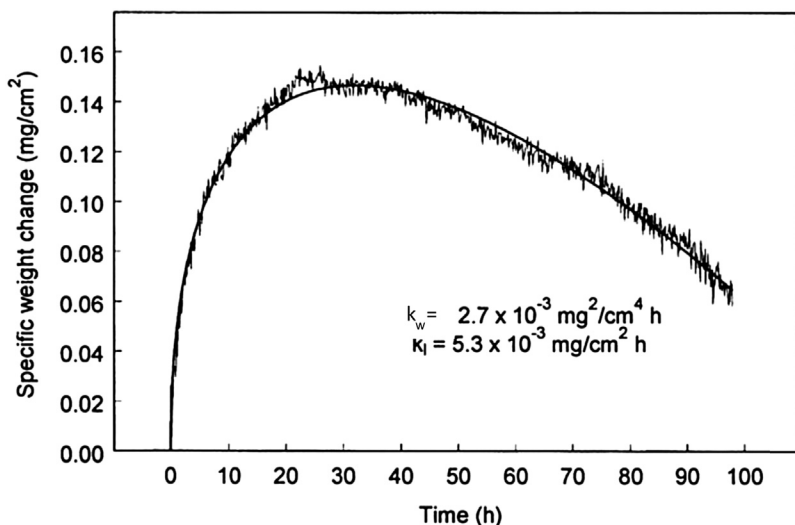


**FIGURE 11.9** Experimentally determined parabolic weight change kinetics for SiC reacted at 1200°C in 50% $\text{H}_2\text{O}$ -50% $\text{O}_2$ . The smooth curve is the result of nonlinear regression on Eqs [11.21] and [11.22]. Published with permission from E.J. Opila, R.E. Hann, *J. Am. Ceram. Soc.* 80 (1997) 197, American Ceramic Society.

which yields

$$t = \frac{k_p}{k_l^2} \left[ -\frac{k_l X}{k_p} - \ln \left( 1 - \frac{k_l X}{k_p} \right) \right] \quad [11.20]$$

The analogous expression for weight uptake

$$t = \frac{\alpha^2 k_w}{(k_l')^2} \left[ -\frac{k_l' \Delta W_1 / A}{\alpha k_w} - \ln \left( 1 - \frac{k_l' \Delta W_1 / A}{\alpha k_w} \right) \right] \quad [11.21]$$

is summed with the expression for evaporative weight loss

$$\Delta W_2 / A = -\beta k_l t \quad [11.22]$$

to obtain the net weight change. Here  $k_w$  is the usual parabolic rate constant for diffusion controlled weight uptake,  $k_l'$  the linear rate constant for evaporative weight loss and  $\alpha = MW_{\text{SiO}_2} / (MW_{\text{O}_2} - MW_c)$  and  $\beta = MW_{\text{SiC}} / MW_{\text{SiO}_2}$  where  $MW$  is the molecular weight of the indicated species. Nonlinear regression of kinetic data on [11.21] and [11.22] is seen in Fig. 11.9 to succeed. Estimates of  $k_l'$  arrived at in this way were equal to rates measured for the volatilisation of bulk silica. Furthermore, these rates were in agreement with evaporation rates calculated from [11.10] for  $\text{Si}(\text{OH})_4$  at temperatures of 1200–1400°C.

The effects of different combustion conditions on silica volatilisation have been examined by Smialek et al. [40–42]. Their results showed that the reducing conditions produced by excess fuel led to  $\text{SiO}$  volatilisation, whereas

the oxidising, humid conditions resulting from combustion with excess air led to  $\text{Si}(\text{OH})_4$  vapour loss.

In comparing results from laboratory reactors with those of high pressure combustion, it is necessary to account for the effects of total pressure on the parameters in [11.10]. The diffusion coefficient  $D_{\text{AB}}$  and the kinematic viscosity  $\nu$  are each inversely proportional to  $P_{\text{T}}$ , leading to an overall pressure dependence of the evaporation rate

$$J_i = \text{const} \cdot p_i P_{\text{T}}^{-\frac{1}{2}} \quad [11.23]$$

Applying equilibrium expressions for reaction [11.17] and



we find

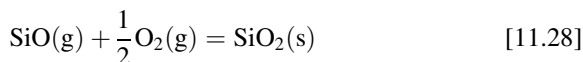
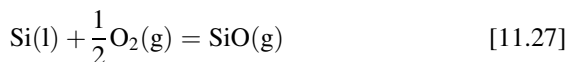
$$J_{\text{SiO}} = \text{const} \cdot P_{\text{T}}^{-\frac{1}{2}} \quad [11.25]$$

$$J_{\text{Si}(\text{OH})_4} = \text{const} \cdot P_{\text{T}}^{\frac{3}{2}} \quad [11.26]$$

Thus increasing the total pressure of a particular gas mixture can alter the relative evaporation rates of  $\text{SiO}$  and  $\text{Si}(\text{OH})_4$ . This was observed in a comparison between  $\text{SiC}$  consumption in a laboratory reactor and high pressure burner rig (Fig. 11.10). Similar results have been found for  $\text{Si}_3\text{N}_4$  [43,44]. Opila [45] has provided maps of  $\text{SiC}$  consumption rates with gas velocity and pressure as ordinates. For typical combustion conditions, rapid recession rates ( $0.2\text{--}2$ )  $\mu\text{m h}^{-1}$  are predicted for  $1200\text{--}1400^\circ\text{C}$ .

### 11.2.5 Silicon Volatilisation

Oxidation of elemental silicon itself leads to vapour formation during metallurgical refining of liquid metal by oxygen blowing to remove calcium and aluminium. The reactions of importance are



In industrial practice, the silica fume formed in this gas-phase reaction consists of amorphous silica spheres of diameter approximately 60 nm. Because the fume constitutes a health hazard, it must be captured, and knowledge of the rate of fume production is therefore required.

Laboratory simulations in which oxygen is flowed over a flat silicon melt surface [46] can be modelled as shown in Fig. 11.11, where oxygen from the bulk gas, with partial pressure  $p_{\text{O}_2}^0$ , diffuses through a hydrodynamic boundary

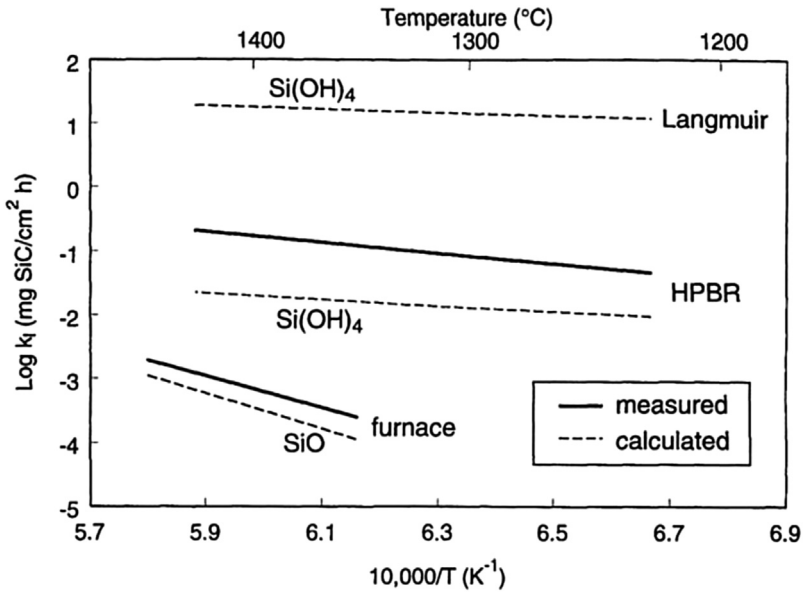


**FIGURE 11.10** Calculated and measured rates of SiC consumption by volatilisation during oxidation in fuel-rich combustion gas. With kind permission from J.L. Smialek, R.C. Robinson, E.J. Opila, D.S. Fox, N.S. Jacobson, *Adv. Compos. Mater.* 8 (1999) 33, Springer Science and Business Media.

layer of thickness  $\delta$  and meets the liquid silicon surface with a partial pressure  $p_{O_2}^s$ . This surface value is very low as a result of the rapid consumption of oxygen via reaction [11.27]. The product  $SiO(g)$ , with surface partial pressure  $p_{SiO}^s$ , diffuses out of the boundary layer. Its bulk partial pressure  $p_{SiO}^0 \approx 0$  as a result of its rapid oxidation via [11.28].

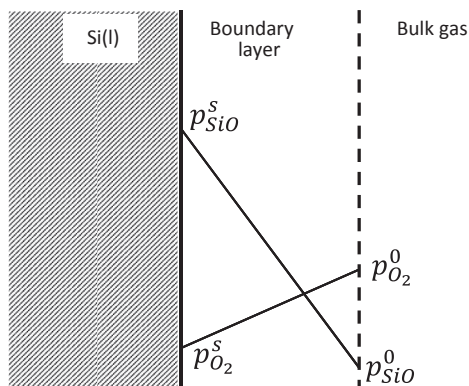


**FIGURE 11.11** Schematic of diffusion profiles in boundary layer of dilute oxygen gas flowing over liquid silicon surface.

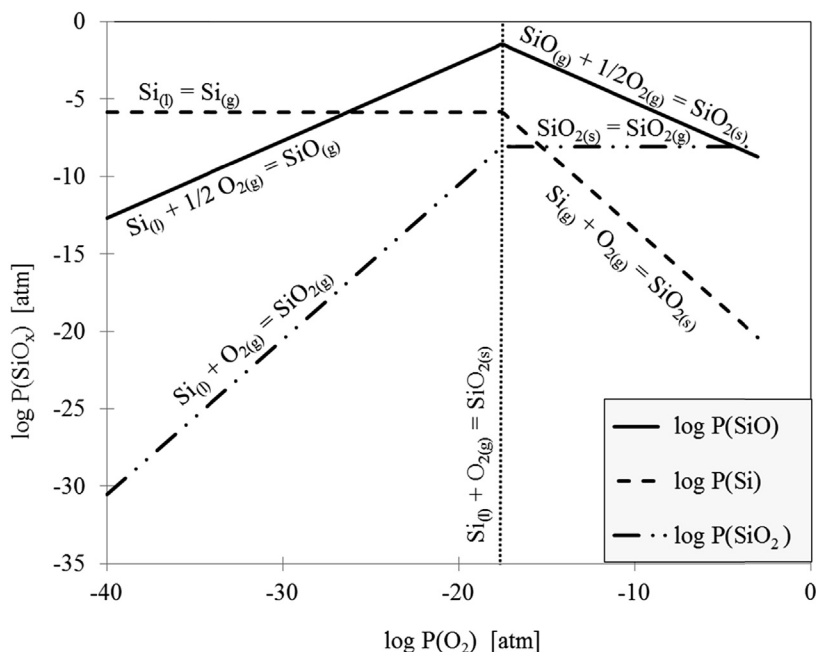


FIGURE 11.12 Thermodynamically calculated partial pressures of  $\text{Si}_{(\text{g})}$ ,  $\text{SiO}_{(\text{g})}$  and  $\text{SiO}_{2(\text{g})}$  as a function of  $p_{\text{O}_2}$  at  $1500^\circ\text{C}$ . M.K. Næss, D.J. Young, J. Zhang, J.E. Olsen, G. Tranell, *Oxid. Met.* 78 (2012) 363, with kind permission from Springer Science and Business Media.

Thermodynamic equilibrium calculations [46] establish the partial pressure of Si-bearing species at  $1500^\circ\text{C}$ , as shown in Fig. 11.12, which illustrates the principal features of the Si–O system. The partial pressure of SiO is controlled by the equilibrium of Eq. [11.27] at oxygen activities too low for solid silica formation. The variation of  $p_{\text{SiO}}^{\text{s}}$  with  $p_{\text{O}_2}^{\text{s}}$  is represented by the solid line in Fig. 11.12 and reaches a maximum at a surface oxygen pressure of  $p_{\text{O}_2}^{\text{s}} = 2.86 \times 10^{-18}$  atm. The corresponding maximum value of  $p_{\text{O}_2}^0$  can be calculated from the theory of mass transfer in the viscous regime, ie, by diffusion across the boundary layer as described by [11.10]. In this way a value of maximum  $p_{\text{O}_2}^0(\text{max}) = 8.6 \times 10^{-3}$  atm at  $1500^\circ\text{C}$  is found. At higher values of  $p_{\text{O}_2}^0$ , faster inward oxygen diffusion leads to  $\text{SiO}_2$  formation and passivation of the surface. Only when  $p_{\text{O}_2}^0 \leq p_{\text{O}_2}^0(\text{max})$  is  $\text{SiO}(\text{g})$  formation kinetically feasible, and the ‘active oxidation’ of silicon predicted by Wagner [47] possible.

Measurements [46] at  $1500^\circ\text{C}$  in dilute Ar– $\text{O}_2$  mixtures flowing at rates of  $2\text{--}14\text{ cm s}^{-1}$  showed that silicon loss rates were proportional to  $p_{\text{O}_2}^0$  and to  $(\nu/L)^{1/2}$ , as predicted from the stoichiometric balance

$$\frac{1}{2}J_{\text{SiO}} = J_{\text{O}_2} \quad [11.29]$$



and Eq. [11.10]. However, the absolute magnitudes of the volatilisation rates were found to be 2–3 times faster than predicted. This difference can be understood from the recognition that Eq. [11.10] applies to boundary layer flow over a flat plate in an otherwise unconstrained space. These experiments, however, were performed in a tubular furnace where the velocity profile is not accurately predicted by the boundary layer theory, because  $\delta$  is significant compared to the tube cross-section.

Computational fluid dynamic (CFD) modelling [46], using an average value of  $\nu = 4.7 \text{ cm}^2 \text{ s}^{-1}$  for the flow fields within a tube containing a flat silicon surface, confirm that flow is indeed laminar, as required for the use of [11.10]. However the CFD model yields enhanced mass transfer coefficient values, accounting for the experimental volatilisation rates being faster than predicted from [11.10]. The essential reason is that an additional hydrodynamic layer is attached to the tube wall, maximum gas velocities are thereby accelerated, and the rate of silicon oxidation is consequently increased.

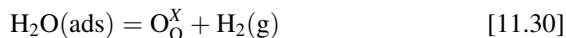
### 11.2.6 Other Oxides

The predominant aluminium hydrate vapour species is  $\text{Al}(\text{OH})_3$  over the temperature range 1100–1900°C [11]. Its partial pressure is low, and vapourisation rates have been measured [11] as  $5 \times 10^{-11}$ – $5 \times 10^{-10} \text{ g (Al) cm}^{-2} \text{ s}^{-1}$  at temperatures of 1250–1500°C in 50%  $\text{H}_2\text{O}$  – 50%  $\text{O}_2$  flowing at  $4.4 \text{ cm s}^{-1}$ . Thus volatilisation is unimportant for alumina-forming alloys at likely service temperatures of up to ca. 1200°C. If alumina-based composites are used at higher temperatures in long-term applications, volatilisation might play a role in limiting material lifetimes.

Zirconia, hafnia and yttria all appear to be exceptionally stable in water vapour-containing environments up to about 1900°C [48–50], but directly measured thermodynamic data are lacking. The successful use of yttria-stabilised zirconia TBCs at surface temperatures exceeding 1200°C confirms the stability of these oxides with respect to any hydrated species.

## 11.3 SCALE-GAS INTERFACIAL PROCESSES

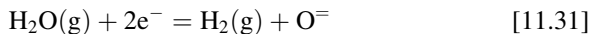
The oxygen uptake reaction at the scale-gas interface is close to equilibrium whenever scale growth kinetics are parabolic and diffusion is rate-controlling. Thus the addition of  $\text{H}_2\text{O}(\text{g})$  to air or oxygen at a fixed  $p_{\text{O}_2}$  value cannot increase the scaling rate by accelerating the scale-gas reaction. However, it could in principle decrease the rate if  $\text{H}_2\text{O}$  adsorption occurred preferentially and if the reaction



were slow. There appear to be no instances of reactions in which scale growth in air or  $\text{O}_2$  plus  $\text{H}_2\text{O}(\text{g})$  is slower than in dry air or oxygen [1,2]. However, if

$\text{H}_2\text{O}(\text{g})$  completely replaces oxygen, then the phase boundary reaction can become rate-controlling if oxide diffusion is rapid.

Turkdogan et al. [51] showed that the growth kinetics of  $\text{Fe}_{1-\delta}\text{O}$  on iron exposed at  $850\text{--}1150^\circ\text{C}$  to  $\text{H}_2/\text{H}_2\text{O}$  mixtures were initially linear and subsequently parabolic. In the early stages of reaction the rate was controlled by an oxide-gas boundary reaction, formulated as



This is similar to [3.133] for oxidation by  $\text{CO}_2$ . A similar kinetic model based on a constant number of adsorption sites per unit area leads to

$$\text{Rate} = k_f \theta_V p_{\text{H}_2\text{O}} \left( 1 - \frac{a'_\text{O}}{a''_\text{O}} \right) \quad [11.32]$$

where, as before,  $\theta_V$  is the fraction of surface sites vacant, and  $a'_\text{O}$ ,  $a''_\text{O}$  are the oxygen activities at the metal-scale and scale-gas interfaces. Initial stage oxidation rates are seen in Fig. 11.13 to vary with gas composition as predicted

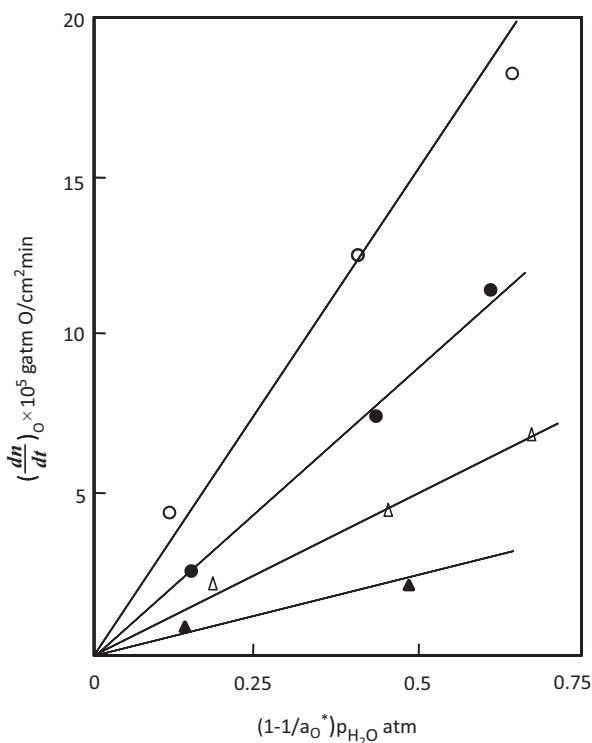
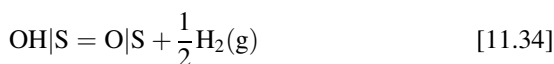
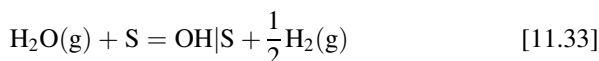


**FIGURE 11.13** Variation of initial linear kinetics for iron oxidation with gas composition according to Eq. [11.32]. Reprinted with permission from E.T. Turkdogan, W.M. McKewan, L. Zwell, *J. Phys. Chem.* 69 (1965) 327, Copyright (1965) American Chemical Society.

by [11.32]. As the scale thickened, diffusion became slower until it controlled the rate and the kinetics became parabolic.

In fact, the reaction [11.31] is rather fast, and an initial period in which the boundary reaction controls the rate is only possible because diffusion in  $\text{Fe}_{1-\delta}\text{O}$  is very rapid. Diffusion in chromia and alumina scales is much slower, and no period of rate control by a reaction such as [11.31] has been reported. On the contrary, the growth of  $\text{Cr}_2\text{O}_3$  scales is faster in  $\text{H}_2\text{O}(\text{g})$  than in  $\text{O}_2$ , as is discussed in Section 11.4.

Galerie et al. [52] have analysed the surface interaction between oxide scales and  $\text{H}_2\text{O}(\text{g})$  in terms of molecular dissociation as affected by the oxide chemistry. If the oxide microstructure and diffusion properties are unchanged by the water vapour, then the surface process becomes important. These authors propose a two-step dissociation process



represented here without considering charge transfer processes. A consideration of bond energies in gaseous  $\text{H}_2\text{O}$  leads to the conclusion that  $\Delta H$  for [11.33] is similar to that of  $\text{O}_2(\text{g})$  dissociation, but  $\Delta H_{34}$  is much larger. Assuming then that [11.34] is slow and rate-controlling, while [11.33] is at equilibrium, we use the methods of Section 2.9 to find the general result

$$\text{Rate} = \frac{k_{31}K_{30}Mp_{\text{H}_2\text{O}}/p_{\text{H}_2}}{1 + K_{30}p_{\text{H}_2\text{O}}/p_{\text{H}_2}} \quad [11.35]$$

with  $M$  the surface concentration of adsorption sites. At low surface coverages, this simplifies to

$$\text{Rate} = k_{31}K_{30}Mp_{\text{H}_2\text{O}}/p_{\text{H}_2} \quad [11.36]$$

and the overall rate clearly depends on both the rate constant  $k_{31}$  and the pre-equilibrium constant  $K_{30}$ .

Galerie et al. [52] suggested that the adsorption constant  $K_{30}$  can be correlated with the enthalpy of oxide cation hydration. In this case the oxygen uptake rate given by [11.33] is predicted to increase as the enthalpy of hydration becomes more negative. Estimates of hydration enthalpies are available from heats of solution and lattice energy calculations. As seen in Table 11.4, there is a small increase in  $|\Delta H_{\text{hyd}}|$  among transition metal cations from  $\text{Cr}^{3+}$  to  $\text{Ni}^{2+}$ , and all have much lower enthalpy changes than that of  $\text{Al}^{3+}$ . The kinetic data for oxide scaling shown in Table 11.4 reveal that  $\text{NiO}$  and  $\text{FeO}$  formed as compact scales in oxygen-free  $\text{H}_2\text{O}(\text{g})$  grow according to linear kinetics. A comparison with a reaction in  $\text{O}_2(\text{g})$  (Fig. 11.14) is consistent with the Galerie model of a slow surface process on these weakly hydrating

TABLE 11.4 Cation Hydration Energies (kJ mol <sup>-1</sup> ) at 298K [53] and Metal Oxidation Kinetics					
Ion	$\Delta H$	Oxidation $T$ (°C)	Metal Oxidation Kinetics		References
			H <sub>2</sub> O(g)	O <sub>2</sub> (g)	
Al <sup>3+</sup>	-4707	980		$k_w = 3 \times 10^{-13a}$	[54]
Cr <sup>3+</sup>	-1883	1000	$k_w = 9 \times 10^{-12a}$	$k_w = 2 \times 10^{-12a}$	[55]
Mn <sup>2+</sup>	-1878				
Fe <sup>2+</sup>	-1954	550	Linear	Parabolic	[56]
Co <sup>2+</sup>	-2088				
Ni <sup>2+</sup>	-2138	800	Linear	Parabolic	[52]

<sup>a</sup>Units: g<sup>2</sup> cm<sup>-4</sup> s<sup>-1</sup>.

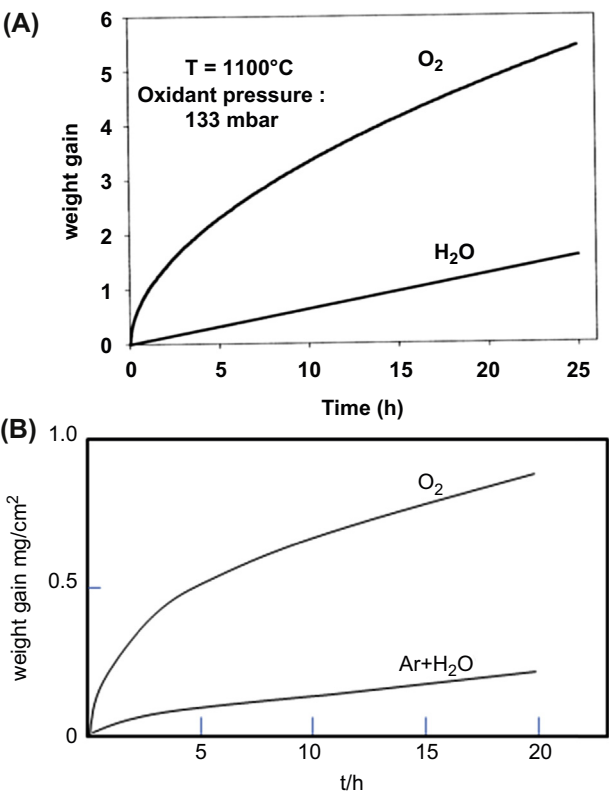


FIGURE 11.14 Oxidation kinetics: (A) nickel at 800°C (published with permission from O.H. Krikorian, *High Temp. High Pressure* 14 (1982) 387, Trans Tech Publications Ltd.) and (B) for iron at 550°C (reprinted with permission from D. Caplan, M. Cohen, *Corros. Sci.* 7 (1967) 725, Elsevier).

oxides. On this basis, it would be predicted that the process would be even slower on  $\text{Cr}_2\text{O}_3$ . However, diffusion in  $\text{Cr}_2\text{O}_3$  is much slower than in  $\text{Fe}_3\text{O}_4$  or  $\text{NiO}$ , and remains rate-controlling during reaction with  $\text{H}_2\text{O}(\text{g})$ . The rate, however, is accelerated. Similarly, the surface reaction would be predicted to be rapid on the strongly hydrating  $\text{Al}_2\text{O}_3$ , and scaling kinetics would therefore be unaffected. Unfortunately, there appear to be no data for alumina growth in nonoxygenated steam. Data for Fe-21.5Cr-5.5Al [54] show that the addition of up to 0.31 atm of  $\text{H}_2\text{O}(\text{g})$  to dry oxygen leads to only a very small decrease in the value of  $k_w$ .

For many oxides, the surface effect discussed above is overwhelmed by the much greater changes in scale microstructure and/or diffusion properties brought about by water vapour. These more important effects are now considered.

## 11.4 SCALE TRANSPORT PROPERTIES

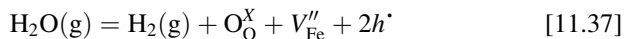
In principle, water vapour can participate in the mass transfer processes within the scale in three different ways: as a gas species within cavities, cracks or voids, as a molecular species and by dissolving hydrogen into the oxide, thereby affecting its lattice point defect concentrations.

### 11.4.1 Gas Transport

Oxidation of low alloy steels and dilute Fe-Cr alloys is frequently observed to produce iron-rich scales containing closed pores and internal fissures. The extent to which scale integrity is lost can be large, as seen in Fig. 11.1B, but still these scales grow rapidly. Pfeil [57] noted that although oxygen anions might be immobile in the oxide lattice, gaseous oxygen could transport across pores and gaps, providing the oxide dissociation pressure is sufficiently high. However, as seen in Section 2.9, the value of  $p_{\text{O}_2}$  in equilibrium with FeO is far too low for the dissociation mechanism to provide a significant contribution to mass transfer [58]. The same conclusion is reached for magnetite scales formed in steam superheater conditions [6] and will obviously apply to more stable oxides such as  $\text{Cr}_2\text{O}_3$  and chromium spinels.

Fujii and Meussner [59,60] observed that  $\text{H}_2\text{O}(\text{g})$  greatly accelerated the oxidation rate of dilute Fe-Cr alloys at 800–1100°C, preventing the formation of a protective chromium-rich scale, promoting instead the growth of FeO plus spinel. Rahmel and Tobolski [61,62] showed that the addition of  $\text{H}_2\text{O}(\text{g})$  to  $\text{O}_2$  slightly accelerated the rate of iron oxidation at 950°C. In both cases, the presence of  $\text{H}_2\text{O}(\text{g})$  caused the scales to develop considerable porosity, and vapour phase transport was considered to be important. Both sets of authors proposed that the presence of  $\text{H}_2\text{O}(\text{g})$  within the pore space would provide the necessary gaseous mass transport. If inward transport of  $\text{H}_2\text{O}(\text{g})$  (or  $\text{H}_2$ ) through the scale and into the pore is relatively fast, then the partial pressure of

$\text{H}_2\text{O}(\text{g})$  in the cavity will approach that of the ambient gas. Oxygen transport is then effected by the reaction



proceeding in the forward direction on the side of a cavity nearest the metal, and in the reverse direction at the outer surface of the cavity. These redox reactions are coupled with gas-phase mass transfer, as shown in Fig. 11.15. Fujii and Meussner [60] calculated that gas-phase transport would provide sufficient oxygen flux to support the observed scaling rates at  $1100^\circ\text{C}$ . The calculation is illustrated here for a lower temperature, where oxygen potentials are much reduced.

At  $650^\circ\text{C}$ , the commercially important 9Cr ferritic-martensitic steels form rapidly growing scales of porous magnetite plus spinel (Fig. 11.1B) when exposed to gases containing water vapour [6,63,64]. The existence range of  $\text{Fe}_3\text{O}_4$  at  $650^\circ\text{C}$  corresponds to oxygen potentials of  $10^{-22}$ – $10^{-13}$  atm, far too low to contribute significantly to mass transport in the cavities. However, if the value  $p_{\text{H}_2\text{O}} = 0.01$  atm is adopted for the cavity interior, one calculates from the thermodynamics of [11.1] that equilibrium  $p_{\text{H}_2}$  values lie in the range  $5 \times 10^{-7}$  to  $10^{-2}$  atm. According to [2.155], these hydrogen pressures can support oxygen transfer rates of  $5 \times 10^{-7}$  to  $10^{-2}$  mol  $\text{cm}^{-2} \text{s}^{-1}$ . These rates are more than enough to support the observed rapid oxygen uptake rates of  $10^{-9}$  mol  $\text{cm}^{-2} \text{s}^{-1}$  accompanying breakaway oxidation (Fig. 11.16).

The contribution of oxygen transport was confirmed by inert marker experiments. Rahmel and Tobolski [61] found platinum markers initially placed on their iron specimens to be located at the metal-scale interface after reaction with dry  $\text{O}_2$ , but within the porous oxide after reaction with  $\text{O}_2 + \text{H}_2\text{O}$ . Scales grown in  $\text{Ar} + \text{H}_2\text{O}$  on iron and Fe-Cr alloys were found by Fujii and

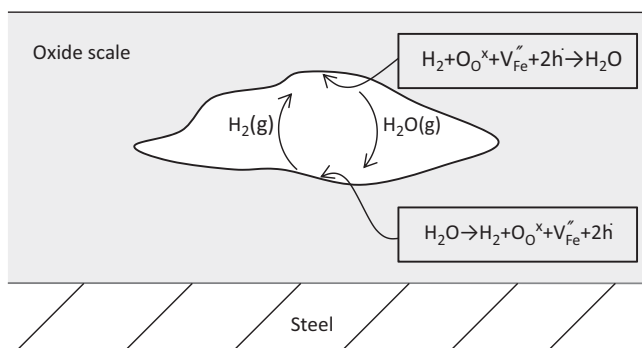


**FIGURE 11.15** Schematic illustration of oxygen transport within a cavity supported by  $\text{H}_2\text{O}(\text{g})$ . Based on A. Dravnieks, H.J. McDonald, *J. Electrochem. Soc.* 94 (1948) 139; C.T. Fujii, R.A. Meussner, *J. Electrochem. Soc.* 110 (1963) 1195; C.T. Fujii, R.A. Meussner, *J. Electrochem. Soc.* 111 (1964) 1215; A. Rahmel, J. Tobolski, *Corros. Sci.* 5 (1965) 333.

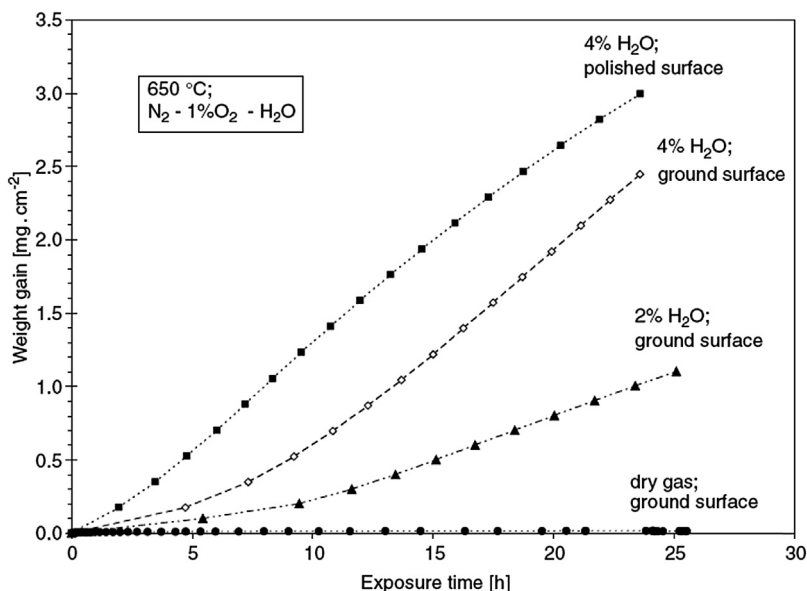


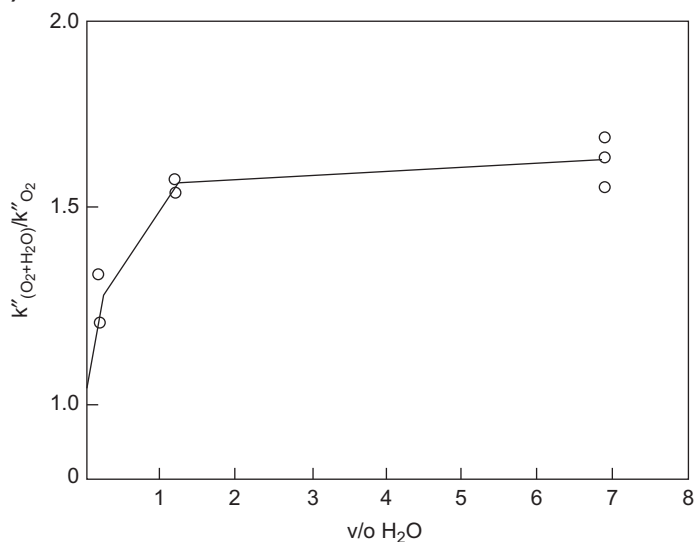
**FIGURE 11.16** Breakaway (rapid) kinetics in isothermal oxidation of 9Cr steel P91 in  $N_2$ -1% $O_2$ - $x$  % $H_2O$  at 650°C. Reprinted from J. Ehlers, D.J. Young, E.J. Smaardijk, A.K. Tyagi, H.J. Penkalla, L. Singheiser, W.J. Quadakkers, *Corros. Sci.* 48 (2006) 3428, with permission from Elsevier.

Meussner [59] to contain platinum markers at the interface between the outer FeO layer and the inner FeO + (Fe,Cr)<sub>3</sub>O<sub>4</sub> layer. In both cases, inward scale growth beneath the marker was attributed to oxygen transport.

The participation of H<sub>2</sub>O in gaseous mass transport within large scale voids thus appears to be firmly established for low alloy steels. The oxidation kinetics were approximately linear, after an initial period of parabolic kinetics. The linear rate constant for iron-rich scale growth on iron and Fe-Cr alloys exposed to Ar-H<sub>2</sub>O gases increased with  $p_{H_2O}^n$ , where  $n = 0.5-0.9$  [60]. However, the effect of  $p_{H_2O}$  on scaling rates in O<sub>2</sub>-H<sub>2</sub>O gases is more complex, as seen in Fig. 11.17. Both iron and the 9Cr steel, P91, oxidised faster when H<sub>2</sub>O was present, but the rate was insensitive to  $p_{H_2O}$  beyond a certain level. In addition, a threshold value of  $p_{H_2O}$  was required to accelerate the rate in Ar-O<sub>2</sub>-H<sub>2</sub>O mixtures, the threshold increasing with  $p_{O_2}$ . This effect is the reason why P91 performs very well at the low  $p_{H_2O}/p_{O_2}$  ratios obtained in laboratory air, but fails at high  $p_{H_2O}$  values. The existence of this effect requires explanation, as do the transport of H<sub>2</sub> or H<sub>2</sub>O into the scale interior and the way in which large voids form when water vapour is present.

Before considering mechanisms of inward hydrogen transport, it is noted that water vapour-induced acceleration of iron oxide scaling is not always accompanied by the development of porous oxide. Tuck et al. [65,66] concluded that the purity of the iron was another factor involved.

(A)



(B)

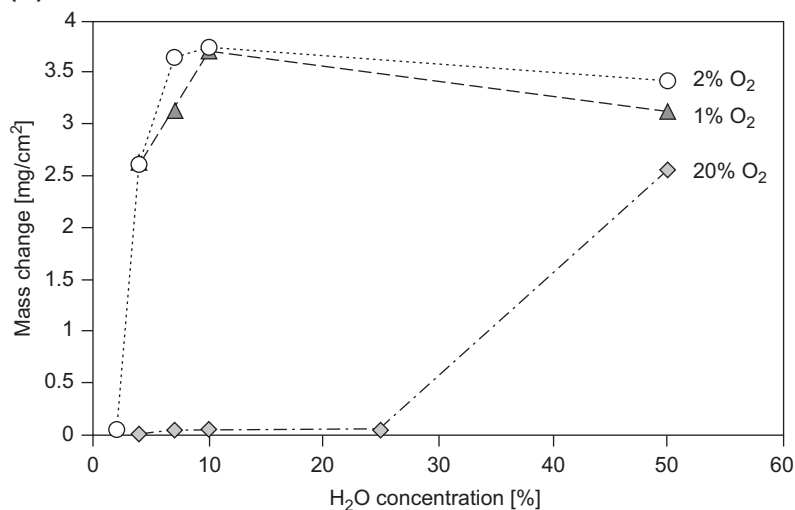


**FIGURE 11.17** Dependence of oxidation behaviour on  $p_{H_2O}$  in  $O_2$  bearing gases: (A) pure Fe in  $O_2 + H_2O$  at  $950^\circ C$  (Reprinted with permission from C.T. Fujii, R.A. Meussner, *J. Electrochem. Soc.* 111 (1964) 1215, The Electrochemical Society) and (B) P91 steel in  $Ar-O_2-H_2O$  at  $650^\circ C$  (Reprinted with permission from J. Ehlers, D.J. Young, E.J. Smaardijk, A.K. Tyagi, H.J. Penkalla, L. Singheiser, W.J. Quadakkers, *Corros. Sci.* 48 (2006) 3428, Elsevier).



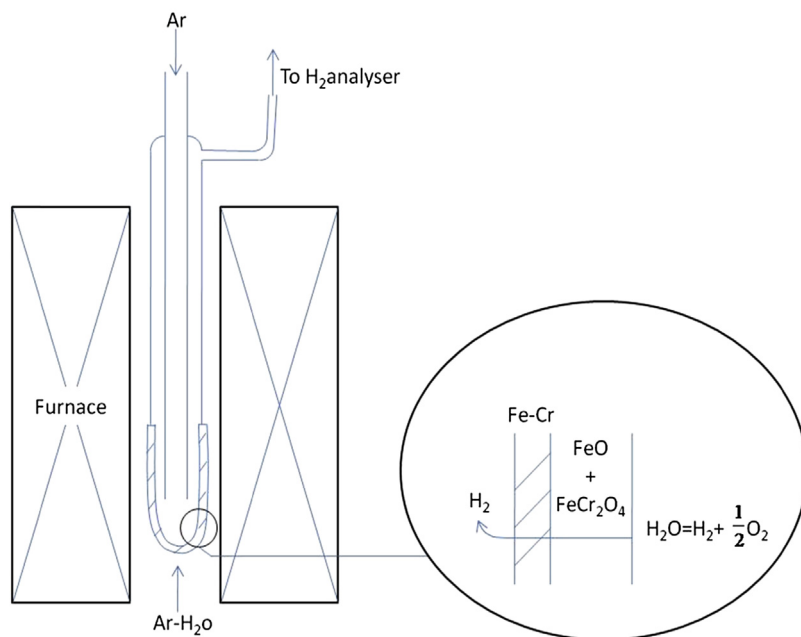


**FIGURE 11.18** Schematic representation of hydrogen transfer experiment described by Fujii and Meussner [59].

The permeability of FeO to hydrogen (or H<sub>2</sub>O(g)) was demonstrated by Fujii and Meussner [60] in the experiment shown in Fig. 11.18. A thin-walled thimble of Fe-5Cr was oxidised on its outside by Ar-10%H<sub>2</sub>O at 1100°C, and the gas in the thimble analysed for hydrogen. A steady flow of hydrogen through the scale (and the alloy) was observed. Rahmel and Tobolski [61] speculated that hydrogen might pass through a wüstite scale as dissolved protons, and Kofstad [1] suggested that it might migrate inwards as water molecules.

### 11.4.2 Molecular Transport

Experiments involving changing the reaction gas from wet to dry and vice-versa are informative. As seen in Fig. 11.19, switching from wet to dry gas after 24 h of breakaway oxidation led to a rapid decrease in the scaling rate observed for the 9% Cr steel, P91. Examination of scale cross-sections after these two stages (Fig. 11.20) reveals that the dry gas caused an increase in the amount of Fe<sub>2</sub>O<sub>3</sub> at the expense of Fe<sub>3</sub>O<sub>4</sub> and densification of the oxide. Thus during the second stage of the experiment, oxygen entered the scale interior where it converted Fe<sub>3</sub>O<sub>4</sub> to Fe<sub>2</sub>O<sub>3</sub>. The volume expansion accompanying this transformation, together with some additional oxide growth, led to much of the pore space being eliminated.

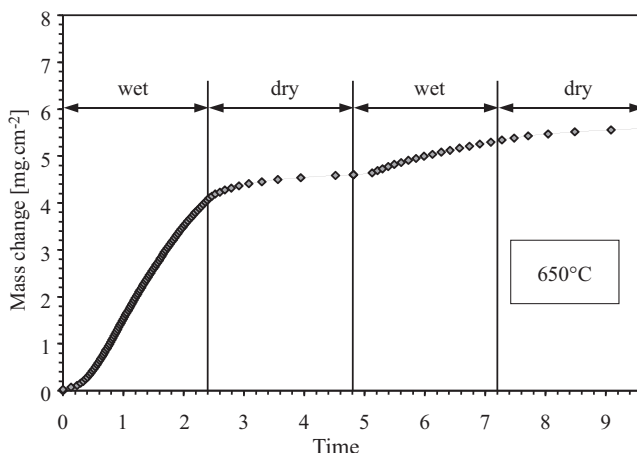


**FIGURE 11.19** Isothermal oxidation kinetics for P91 (a 9% Cr steel) at 650°C when gas alternated between  $N_2$ -1% $O_2$ -4% $H_2O$  and  $N_2$ -1% $O_2$  every 24 h. Reprinted from J. Ehlers, D.J. Young, E.J. Smaardijk, A.K. Tyagi, H.J. Penkalla, L. Singheiser, W.J. Quadackers, *Corros. Sci.* 48 (2006) 3428, with permission from Elsevier.

For this to occur, the scale originally grown in wet gas (Fig. 11.20A) must have been permeable to gas species. The outer  $Fe_2O_3$  layer, despite its compact appearance, must have allowed inward gas species diffusion. Since, nevertheless, a large gradient in oxygen activity was maintained (as shown by the sequential distribution of oxide phases), this diffusion process must have been much slower than gas-phase transport. Molecular diffusion along internal surfaces, such as grain boundaries, would provide a suitable transport mechanism [6].

Commencing the experiment in dry rather than wet gas led to very different results [6]. A protective scale of  $Fe_2O_3$  on top of chromium-rich spinel grew in dry gas and was not affected, at least for some days, by subsequent exposure to the wet gas. However, if the scale was cooled and reheated, the coefficient of thermal expansion difference between scale and metal led to scale damage and subsequent rapid reaction in wet gas. Thus the  $Fe_2O_3$  grown during isothermal exposure to dry gas was not subsequently permeable to  $H_2O(g)$  in the time scale of the experiment. Unlike the scale grown in wet gas, the oxide grown in dry gas appeared to be fully dense as long as no scale damage was introduced. Schutze et al. [69] also found breakaway of the initially formed protective scale on P91 to occur only in association with scale damage, as detected by acoustic emission analysis.

Reaction of the P91 steel with an isotopically labelled gas mixture  $N_2$ -1% $^{16}O_2$ -2% $H_2^{18}O$  and subsequent analysis of isotope profiles in the scale led to the results shown in Fig. 1.17. It was found that  $^{16}O$  from molecular oxygen was always more abundant than  $^{18}O$  from  $H_2O$  in the inner part of the scale. In the outer part of the scale, the two isotopes were present at

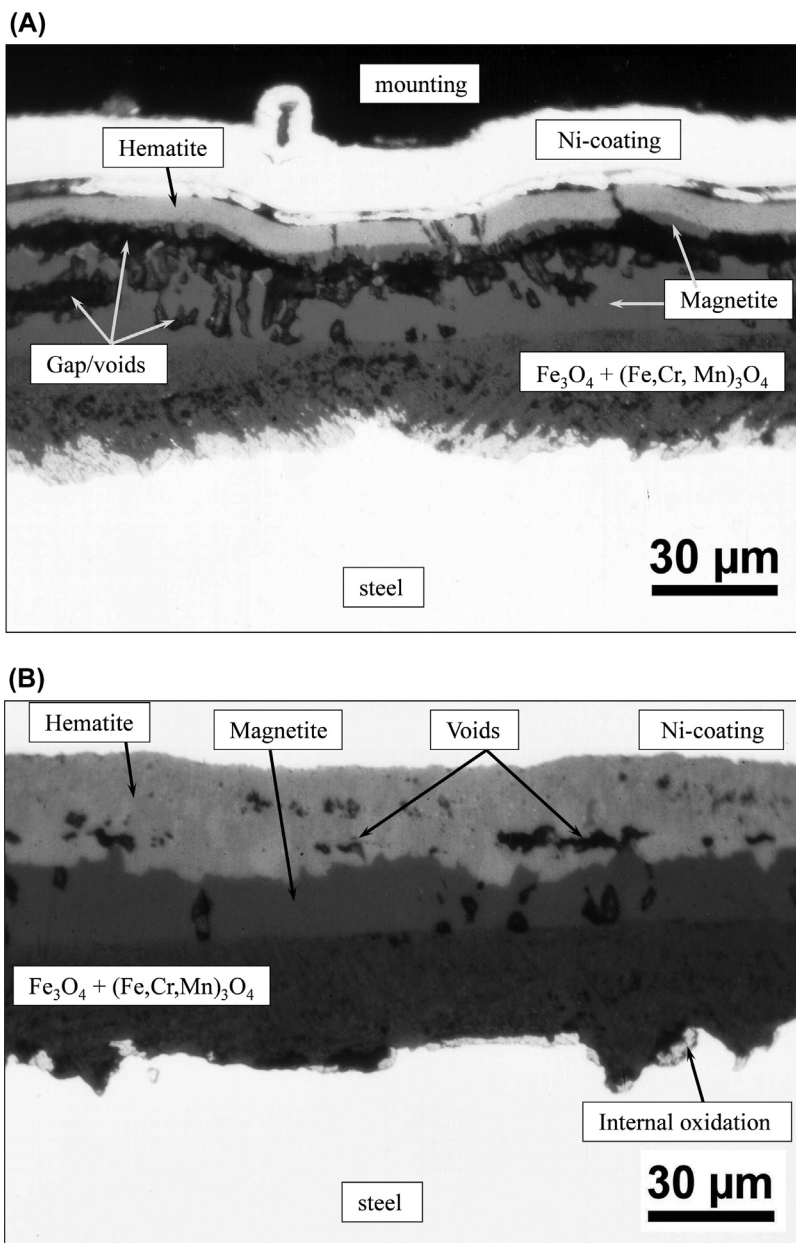


**FIGURE 11.20** Cross-section of scales grown on P91 after reaction stages shown in Fig. 11.19: (A) 24 h and (B) 48 h. Reprinted from J. Ehlers, D.J. Young, E.J. Smaardijk, A.K. Tyagi, H.J. Penkalla, L. Singheiser, W.J. Quadackers, *Corros. Sci.* 48 (2006) 3428, with permission from Elsevier.

approximately equal concentrations in a prebreakaway scale, but  $^{18}\text{O}$  was enriched in this region after breakaway. These distributions confirm that when water vapour is present at a sufficient level, some of its oxygen content is incorporated into the scale interior, consistent with inward diffusion of a molecular species through the outer part of the scale. The different isotope distributions also show that oxygen in the presence of water vapour does not react with (and thereby densify) the outer scale. Instead, reaction with  $\text{H}_2\text{O}(\text{g})$  is favoured in this region.

The competition between  $\text{O}_2$  and  $\text{H}_2\text{O}$  induced oxidation reactions is also evident in Fig. 11.17B, where the condition for breakaway oxidation can be approximated [6] as

$$p_{\text{H}_2\text{O}}/p_{\text{O}_2} > 1 \quad [11.38]$$

Hayashi and Narita [70] also proposed that the change from slow to rapid oxidation of Fe-5Al alloys at  $800^\circ\text{C}$  depended on the  $p_{\text{H}_2\text{O}}/p_{\text{O}_2}$  ratio. A simple qualitative interpretation of these findings is that a minimum  $p_{\text{H}_2\text{O}}/p_{\text{O}_2}$  ratio is required for sufficient  $\text{H}_2\text{O}(\text{g})$  to enter the scale and lead to breakaway oxidation.

If molecules species enter the scale by adsorption on internal surface sites, S, we can write



where dissociative adsorption has been ignored. Treating the adsorption equilibria using the methods of Section 2.9, one finds

$$[\text{H}_2\text{O}|\text{S}] = \frac{M K_{39} p_{\text{H}_2\text{O}}}{1 + K_{39} p_{\text{H}_2\text{O}} + K_{40} p_{\text{O}_2}} \quad [11.41]$$

$$[\text{O}_2|\text{S}] = \frac{M K_{40} p_{\text{O}_2}}{1 + K_{39} p_{\text{H}_2\text{O}} + K_{40} p_{\text{O}_2}} \quad [11.42]$$

with  $M$  the assumed constant concentration of surface sites. It follows immediately that

$$\frac{[\text{H}_2\text{O}|\text{S}]}{[\text{O}_2|\text{S}]} = \frac{K_{36} p_{\text{H}_2\text{O}}}{K_{40} p_{\text{O}_2}} \quad [11.43]$$

This competitive adsorption process provides an explanation for the finding that higher  $p_{\text{O}_2}$  values require higher  $p_{\text{H}_2\text{O}}$  values to bring about breakaway oxidation, as expressed in [11.38].

When [11.38] is satisfied, it is likely that adsorption of the polar  $\text{H}_2\text{O}$  molecule predominates, and [11.41] can be approximated by

$$[\text{H}_2\text{O}|\text{S}] \approx \frac{M K_{39} p_{\text{H}_2\text{O}}}{1 + K_{39} p_{\text{H}_2\text{O}}} \quad [11.44]$$

It is clear from this result that at sufficiently high  $p_{\text{H}_2\text{O}}$  values, the surfaces saturate with  $\text{H}_2\text{O}(\text{ads})$ , and the rate of reaction between this species and the scale would be independent of  $p_{\text{H}_2\text{O}}$ . This would explain the insensitivity of breakaway rates to  $p_{\text{H}_2\text{O}}$  (Fig. 11.17). It should be noted, however, that  $K_{38}$  and  $K_{39}$  are temperature-dependent, and the condition [11.38] is therefore expected to have different values for its right-hand member at different temperatures. Thus relatively small additions of  $\text{H}_2\text{O}(\text{g})$  to air are sufficient at  $980^\circ\text{C}$  to induce rapid breakaway oxidation of Fe-13Cr and Fe-13Cr-2Al alloys [31].

The competitive adsorption process is also consistent with the isotope distribution experiments (Fig. 1.17), which showed that in the breakaway regime, oxygen from water vapour was the major species incorporated into the outer scale and molecular oxygen the major species taken up by the inner scale. The preferential adsorption of  $\text{H}_2\text{O}(\text{g})$  in the outer part of the scale largely excludes the  $\text{O}_2$  species from the surface and thereby reduces its uptake. Only deep within the scale, beyond the part at which most of the  $\text{H}_2\text{O}(\text{g})$  has been consumed, is  $\text{O}_2$  an effective reactant. In addition, the competitive adsorption process explains the ability of scales formed in breakaway-inducing atmospheres to resist densification and retain their gas permeability. Adsorbed  $\text{H}_2\text{O}$  excludes  $\text{O}_2$  from the internal surfaces of the outer scale region, whilst itself reacting only relatively slowly. Only when  $\text{H}_2\text{O}$  is removed from the gas phase can  $\text{O}_2$  gain access to these surfaces. Finally, the adsorption model is consistent with the finding that dense, protective scales grown in dry oxygen are not subsequently permeated by  $\text{H}_2\text{O}(\text{g})$ . In the absence of internal surfaces, adsorption and penetration of molecular  $\text{H}_2\text{O}(\text{g})$  is not possible.

Silica scales are usually amorphous, or glassy, and therefore contain no grain boundaries. Nonetheless, additions of water vapour to oxygen greatly accelerate the rate of silicon oxidation [67]. The activation energy is decreased, and becomes equal to that observed for the permeability of  $\text{H}_2\text{O}$  in silica [68]. The effect is due to the silica network-modifying effect of the OH species.

### 11.4.3 Molecular Transport in Chromia Scales

Provided that the temperature and gas velocity are not too high, the term  $k_v$  in [1.36] is small, and the early stages of chromia scale growth in  $\text{O}_2 + \text{H}_2\text{O}$  gases are close to parabolic in their kinetics. Despite the unimportance of the volatilisation process at this stage, the presence of  $\text{H}_2\text{O}(\text{g})$  nonetheless affects significantly the short-term diffusion-controlled oxidation rate. Tveten and Hultquist [71–73] examined the effect of alloy impurity hydrogen on the oxidation of chromium-base alloys in pure oxygen and water vapour. The adhesion of scales grown in pure oxygen was very poor. Scales grown in  $\text{H}_2\text{O}(\text{g})$  were much more adherent and grew more quickly. Quadakkers et al. [74] reported the similar finding that scales formed on chromium-base alloys in Ar- $\text{H}_2$ - $\text{H}_2\text{O}$  were more adherent than those grown in air. Michalik et al. [75] also found that oxide scale adherence on pure chromium depends on the oxygen and water vapour partial pressures of the reaction gas.

Leaving the discussion of the variation of  $k_p$  with  $p_{O_2}$  and  $p_{H_2O}$  in  $H_2/H_2O$  atmospheres for the subsequent section, we consider first the reasons for the differences between reactions in wet and dry atmospheres. Observations of chromia scale growth on Ni-Cr alloys are of use in analysing this issue.

Isothermal oxidation of Ni-25Cr at 1000°C led to the short-term parabolic rate constant values shown in Fig. 11.21. Steady-state values of  $k_w$  were higher for this alloy in Ar-4% $H_2$ -7% $H_2O$  than in Ar-20% $H_2O$ . The addition of yttrium to the alloy decreased the rate in Ar- $O_2$ , but slightly increased the rate in Ar- $H_2$ - $H_2O$ . Scales formed on both NiCr and NiCrY in Ar- $H_2$ - $H_2O$  were considerably thicker and exhibited better adherence to their substrates than

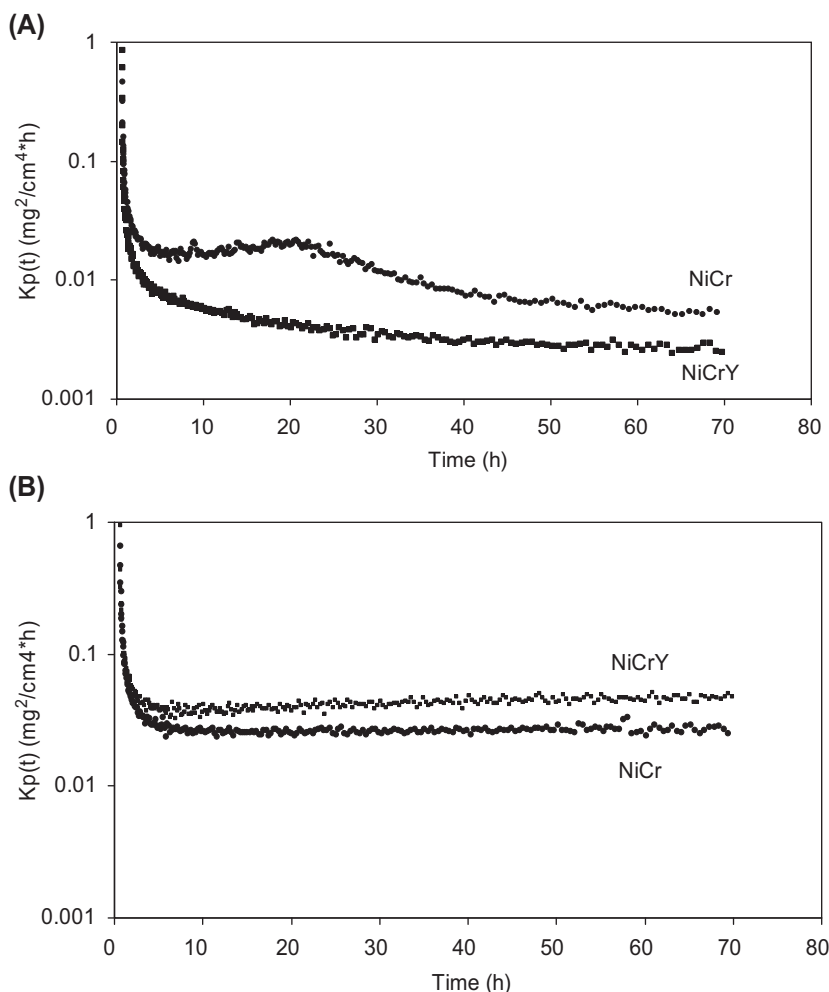


**FIGURE 11.21** Instantaneous parabolic rate constant for Ni-25Cr and Ni-25Cr-0.1Y at 1000°C: (A) in Ar-20% $O_2$  (B) in Ar-4% $H_2$ -7% $H_2O$ . Reprinted from J. Zurek, D.J. Young, E. Essuman, M. Hänsel, H.J. Penkalla, L. Niewolak, W.J. Quadackers, *Mater. Sci. Eng. A* 477 (2008) 259–270, with permission from Elsevier.

those grown in Ar-O<sub>2</sub>. Part of the explanation for these effects lies in the different diffusion mechanisms.

Two-stage oxidation experiments using Ar-<sup>16</sup>O<sub>2</sub> (or Ar-H<sub>2</sub>-H<sub>2</sub><sup>16</sup>O) followed by Ar-<sup>18</sup>O<sub>2</sub> (or Ar-H<sub>2</sub>-H<sub>2</sub><sup>18</sup>O) led to the isotope distributions shown in Fig. 11.22. Normalised plots are used for the scale grown in Ar-O<sub>2</sub> to compensate for the partial spallation which occurred on cooling. The profiles after Ar-O<sub>2</sub> exposure show the well-known tracer distribution found for scales growing by cation diffusion [77–79]. Thus the oxygen in the outer scale is nearly exclusively <sup>18</sup>O. Its concentration is seen to be approximately constant in the outer region, and then decreases rapidly to a low level in the inner region.

After two-stage oxidation in Ar-H<sub>2</sub>-H<sub>2</sub>O, a substantial part of the <sup>18</sup>O is again present in the outer part of the scale, but no region of constant concentration is found. Instead, the concentration decreases continuously as a function of sputter time and shows a minor enrichment at the scale-alloy interface. This distribution indicates that scale growth proceeds by inward oxygen transport. The same conclusion was reached by Hultquist et al. [73] for pure chromium oxidised in H<sub>2</sub>O(g).

The Cr<sub>2</sub>O<sub>3</sub> scale grown in Ar-O<sub>2</sub> developed pores and voids at and near the oxide-alloy interface. Michalik et al. [75] proposed that this was due to condensation of vacancies left by outwardly diffusing metal. In contrast, the chromia scale grown in Ar-H<sub>2</sub>-H<sub>2</sub>O was compact and closely adherent to the substrate alloy. As shown earlier, water vapour can eliminate or at least decrease oxide porosity by providing rapid gas-phase transport of oxygen within the pore space. Furthermore, inward oxygen transport leads to new oxide formation at the scale-metal interface, thereby reducing the probability of void nucleation and subsequent scale detachment. The inward oxygen transport revealed by isotope-profiling experiments in the case of Ar-H<sub>2</sub>-H<sub>2</sub>O reaction accounts satisfactorily for the observed decrease in scale porosity and improved scale adhesion, if the diffusing species contains both oxygen and hydrogen, either hydroxyl ions [52] or H<sub>2</sub>O(ads).

As discussed in Section 4.2, chromia scales grown in dry gases were found to be permeable to nitrogen but impermeable when the gas contained water vapour. This led to the suggestion that water vapour interacted with scale grain boundaries, affecting their ability to transmit molecular species. The oxide grain structures developed on Ni-25Cr are seen in Fig. 11.23 to be quite different in the presence and absence of water vapour. The scale formed in Ar-O<sub>2</sub> has large, rather columnar grains, whereas the oxide grown in Ar-H<sub>2</sub>-H<sub>2</sub>O is extremely fine-grained, with some increase in grain size towards the alloy side. The much finer grain size would provide a greater contribution to mass transport by inward grain boundary diffusion, thereby accounting for the faster scaling rate observed in this gas (Fig. 11.21). The remaining question concerns the way in which H<sub>2</sub>O(g) (or H<sub>2</sub>(g)) alters the grain size.

One possibility is that the presence of H<sub>2</sub>O(ads) at the oxide grain boundaries hinders their movement and thus grain growth. This would explain the extremely fine oxide grains formed in Ar-H<sub>2</sub>-H<sub>2</sub>O. One might, however,

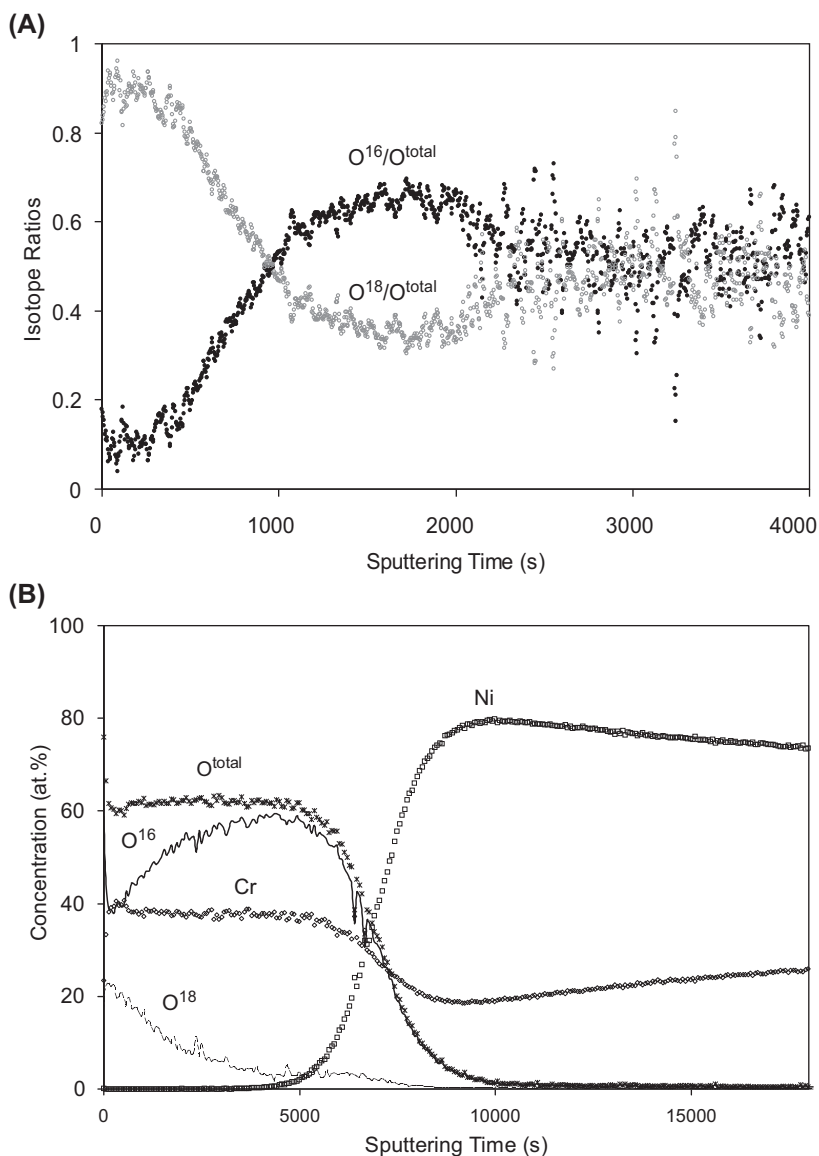
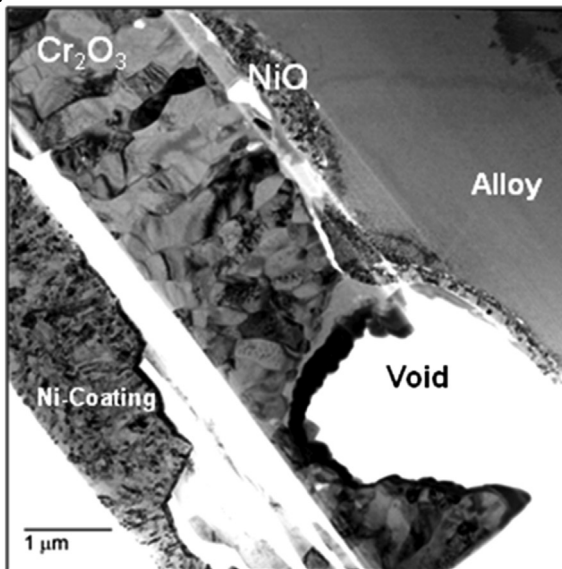


**FIGURE 11.22** Oxygen isotope profiles measured by SNMS after oxidation at 1050°C of Ni-25Cr: (A) first stage 0.5 h in Ar-20%  $^{16}O_2$ , second stage 2 h in Ar-20%  $^{18}O_2$ ; (B) first stage 0.5 h in Ar-4%  $H_2$ -2%  $H_2^{16}O$ , second stage 2 h in Ar-4%  $H_2$ -2%  $H_2^{18}O$ . Reprinted from J. Zurek, D.J. Young, E. Essuman, M. Hänsel, H.J. Penkalla, L. Niewolak, W.J. Quadackers, *Mater. Sci. Eng. A* 477 (2008) 259–270, with permission from Elsevier.



(A)



(B)

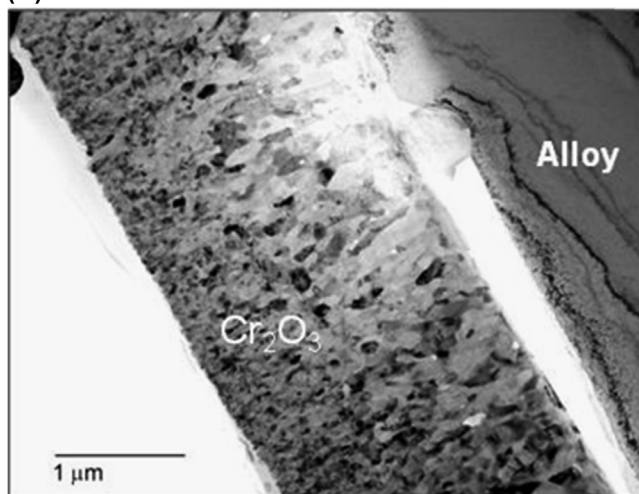


**FIGURE 11.23** TEM bright field views of scale cross-sections developed on Ni-25Cr in 2.5 h at 1050°C (A) in Ar-O<sub>2</sub> (B) in Ar-H<sub>2</sub>-H<sub>2</sub>O. Reprinted from J. Zurek, D.J. Young, E. Essuman, M. Hänsel, H.J. Penkalla, L. Niewolak, W.J. Quadakkers, *Mater. Sci. Eng. A* 477 (2008) 259–270, with permission from Elsevier.

also argue the converse. The stronger contribution of inward scale growth might not be the result of the finer grain size: rather, the finer grain size could result from the modified scale growth process induced by Ar-H<sub>2</sub>-H<sub>2</sub>O gas. In the case of scales mainly growing by cation diffusion, the oxide grains at the free oxide surface can easily form and grow in size without any constraints, whereas during scale growth at the scale/oxide interface, nucleation of new grains might occur more easily than growth of existing grains. The available results do not allow a distinction to be drawn between the two possibilities. Nonetheless, it is clear that the effect of water vapour during oxidation in Ar-H<sub>2</sub>-H<sub>2</sub>O environments is twofold: water molecules incorporated into the scale provide accelerated mass transport within voids whilst simultaneously promoting the formation of an inwardly growing, fine-grained oxide scale.

The complex effects of yttrium additions (Fig. 11.21) can now be understood. In the dry gas, yttrium addition had the expected effect of reducing the rate. As discussed in Section 7.5, yttrium and other reactive element metals segregate to oxide grain boundaries modifying their properties. Grain boundary cation diffusion is largely suppressed, and a slower rate of scale growth is supported by inward oxygen transport. On the other hand, scales formed on Ni-25Cr in Ar-H<sub>2</sub>-H<sub>2</sub>O grow mainly by inward diffusion, and the addition of yttrium cannot decrease the rate by lowering cation diffusion. The small increase in  $k_w$  observed (Fig. 11.21) for NiCrY was attributed to internal oxidation of yttrium.

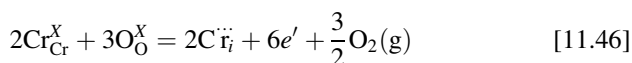
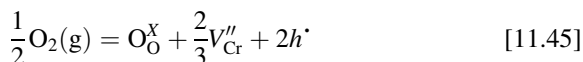
It is seen that water vapour and alloy yttrium have qualitatively similar effects on chromia scale growth. In addition to the mass transport changes discussed above, both lead to oxide grain refinement ([80–82] and Fig. 11.23). Furthermore, in both cases, grain size increases in the growth direction, ie, towards the scale-metal interface. Water vapour is apparently a more effective grain refiner, leading to a higher value of  $D_{\text{eff}}$  (Section 3.9) and somewhat more rapid scaling. The changes in mass transport mechanism brought about by both water vapour and alloy yttrium have the same result of improving scale adherence. Despite these benefits, water vapour is ultimately destructive in its promotion of chromium volatilisation, which degrades the scale in the long-term.

The results reviewed here have led to the conclusion that both oxygen and hydrogen are transported inwards through growing scales of both chromium and iron-rich oxides. Direct evidence for the passage of hydrogen is provided by the experiment shown in Fig. 11.18 for the scale on Fe-5Cr. The accumulation of hydrogen in an Fe-10Cr steel during oxidation in steam has been demonstrated by Nakai et al. [83], and in the chromia scale on a 430 stainless steel (Fe-16Cr-0.5Mn) by Yamauchi et al. [84], using thermal desorption spectroscopy to analyse for hydrogen. Although the evidence is clear, it does not reveal the chemical form of the diffusing entity, H<sub>2</sub>O(ads) or OH<sup>-</sup> ions. The possibility of hydrogen transport via ionic species is now considered.

### 11.4.4 Ionic Transport

Interactions between water vapour and ionic point defects in oxides have been studied in a number of oxides [1,2], but attention is focused here on chromia scales. Not only are they important, but a significant amount of data is available. Unfortunately, because  $\text{Cr}_2\text{O}_3$  is so closely stoichiometric, and its intrinsic defect concentrations so low, the defect behaviour is poorly defined. It seems (Section 3.9) that both metal excess and metal deficit behaviour are possible in appropriate oxygen potential ranges.

Consider first the principal point defect formation reactions involving cation vacancy and interstitial formation in  $\text{Cr}_2\text{O}_3$



In the case of vacancy formation, the charge balance

$$[h^{\cdot}] = 3[V_{\text{Cr}}'''] \quad [11.47]$$

combined with the equilibrium expression for [11.45] leads to

$$[V_{\text{Cr}}'''] = \left(\frac{K_{42}}{9}\right)^{\frac{3}{8}} p_{\text{O}_2}^{\frac{3}{16}} \quad [11.48]$$

Wagner's theory of diffusion control by lattice defects (Section 3.6) then leads to the scaling constant

$$k_p = \text{const} \cdot \left[ \left(p_{\text{O}_2}''\right)^{\frac{3}{16}} - \left(p_{\text{O}_2}'\right)^{\frac{3}{16}} \right] \quad [11.49]$$

If, instead, the predominant defects are interstitials, the charge balance

$$[e'] = [3\text{Cr}_i^{\cdot\cdot}] \quad [11.50]$$

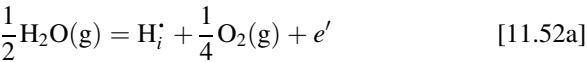
leads to

$$k_p = \text{const} \cdot \left[ \left(\frac{1}{p_{\text{O}_2}'}\right)^{\frac{3}{16}} - \left(\frac{1}{p_{\text{O}_2}''}\right)^{\frac{3}{16}} \right] \quad [11.51]$$

Since  $p_{\text{O}_2}''$  is usually much greater than  $p_{\text{O}_2}'$ , both [11.49] and [11.51] are easily simplified. If vacancies predominate, the rate is predicted to increase with  $p_{\text{O}_2}^{\frac{3}{16}}$ . If interstitials predominate, the rate is almost independent of  $p_{\text{O}_2}$ .

Comparisons [55,76] of experimental data with these predictions have shown that they fail in both  $\text{O}_2/\text{H}_2\text{O}$  and  $\text{H}_2/\text{H}_2\text{O}$  atmospheres. However,

Norby et al. [72,85,86] followed early work on other oxides (eg, [1,87–90]) in suggesting that hydrogen can be injected into the lattice as a proton:



or, equivalently,



Combination of equilibrium expressions for [11.45] and [11.52b] with the charge balance expression

$$3[V_{\text{Cr}}'''] = [h^\cdot] + [\text{H}_i^\cdot] \quad [11.53]$$

leads to the prediction that  $k_p$  increases with  $p_{\text{H}_2}$  at constant oxygen potential and decreases with  $p_{\text{H}_2}$  at constant  $p_{\text{H}_2\text{O}}$ . However, the latter prediction is at variance with the results for pure chromium in  $\text{H}_2/\text{H}_2\text{O}$  atmospheres (Table 11.5), and this model cannot be used. Nonetheless, increasing  $p_{\text{H}_2\text{O}}$  (and  $p_{\text{H}_2}$ ), whilst maintaining  $p_{\text{O}_2}$  constant, does increase the scaling rate (Table 11.5).

If the hydrogen effect is modelled as a hydroxyl species formation



together with a charge balance

$$3[V_{\text{Cr}}'''] = [\text{OH}_{\text{O}}^\cdot] + [h^\cdot] \quad [11.55]$$

then the equilibrium expression for vacancy formation leads to

$$[V_{\text{Cr}}'''] = k_1 p_{\text{O}_2}^{\frac{3}{16}} \left( 1 + k_2 p_{\text{H}_2}^{\frac{1}{2}} \right)^{\frac{3}{4}} \quad [11.56]$$

TABLE 11.5 Oxidation Rate Constants for Pure Cr at 1000°C [55]			
Inlet gas	$p_{\text{O}_2}$ (atm)	$p_{\text{H}_2\text{O}}$ (atm)	$k_w$ ( $\text{g}^2 \text{cm}^{-4} \text{s}^{-2}$ )
Ar-4%H <sub>2</sub> -2%H <sub>2</sub> O	$7.0 \times 10^{-16}$	0.02	$2.0 \times 10^{-11}$
Ar-4%H <sub>2</sub> -4%H <sub>2</sub> O	$2.8 \times 10^{-15}$	0.04	$2.2 \times 10^{-11}$
Ar-4%H <sub>2</sub> -8%H <sub>2</sub> O	$1.1 \times 10^{-14}$	0.08	$7.0 \times 10^{-11}$
Ar-8%H <sub>2</sub> -8%H <sub>2</sub> O	$2.8 \times 10^{-15}$	0.08	$8.6 \times 10^{-11}$
Ar-8%H <sub>2</sub> -4%H <sub>2</sub> O	$7.0 \times 10^{-16}$	0.04	$6.7 \times 10^{-11}$
Ar-4%O <sub>2</sub> -4%H <sub>2</sub> O	0.04	0.04	$1.9 \times 10^{-11}$
Ar-4%O <sub>2</sub> -8%H <sub>2</sub> O	0.04	0.08	$2.0 \times 10^{-11}$

where  $k_1, k_2$  are constants, and the  $\text{H}_2\text{O}(\text{g})$  dissociation equilibrium has been used. Despite some successes, this model fails to account for the observed (Table 11.5) increase in rate with increasing  $p_{\text{H}_2}$  at fixed  $p_{\text{H}_2\text{O}}$  levels. Similarly, it can be shown [55] that a model based on hydrogen or water molecule penetration of an  $n$ -type scale leading to negative hydride formation



leads to an expression for  $[\text{Cr}_i^{\cdot\cdot}]$  which correctly predicts the observed increase in rate with  $p_{\text{H}_2}$  at fixed  $p_{\text{H}_2\text{O}}$ . However, it fails to predict the observed rate dependence on  $p_{\text{H}_2\text{O}}$  at fixed  $p_{\text{H}_2}$ .

It must be concluded that no single defect model explains the observed range of gas composition effects on chromium oxidation. However, a linear combination of mass transfer contributions by  $\text{Cr}_i^{\cdot\cdot}$  and  $V_{\text{Cr}}'''$  together with a hydrogen dissolution equilibrium



does describe the gas compositional dependencies observed at low oxygen activities. The model contains many undetermined constants and lacks quantitative value. However, it does show that an ionic transport model for chromia can only succeed if scale uptake of  $\text{H}_2$  or  $\text{H}_2\text{O}$  is incorporated.

It might be objected that a consideration of lattice point defect chemistry is inappropriate to the case of chromia scales, the growth of which is supported by grain boundary diffusion. This objection is dealt with formally by invoking local equilibrium between grain boundary and lattice, for example



where the subscripts gb and L denote grain boundary and lattice sites, respectively. Thus a gradient in lattice species concentration is accompanied by one in the grain boundaries, where mass transfer actually occurs. Such a formalism does not provide a complete description, as it does not encompass the molecular species which can exist at grain boundaries, but not in the lattice.

#### 11.4.5 Relative Importance of Different Water Vapour Effects on Chromia Scaling

There is no single publication (or set of publications from the same laboratory) describing all the water vapour effects: volatilisation, chromia scale microstructural change, alterations to the relative contributions of oxygen and metal diffusion, and hydrogen doping. This makes for difficulty in assessing the relative magnitude of the different effects, because kinetic data for chromium oxidation vary so widely from one measurement to another (Fig. 3.20). This

variability is understandable. Because  $\text{Cr}_2\text{O}_3$  has such a low intrinsic defect level, grain boundary diffusion predominates and is therefore sensitive to oxide scale microstructure and the present of dopants and boundary segregants. Minor variations in metal and gas purity, which lead to different oxide microstructures and dopant levels, are therefore of critical importance to the observed oxidation rates. Comparisons should therefore be restricted to results obtained with the same material and surface preparation.

Several measurements of parabolic scaling rates for chromia growth in dry oxygen at  $1000^\circ\text{C}$  shown in Table 11.6 illustrate the variability. It is expected, however, that volatilisation from the scale surface would be largely independent of scale microstructure and doping level. Vaporisation losses calculated from [11.10] for  $\text{CrO}_2(\text{OH})_2$  formation in air-10%  $\text{H}_2\text{O}(\text{g})$  flowing at  $2\text{ cm s}^{-1}$  are shown in the table as fractions of the scale thicknesses. It is seen that volatilisation can be neglected for short-term laboratory experiments, even in the case of the remarkably slow scaling rates measured by Caplan and Cohen [56].

However, the changes made by water vapour to the microstructure and transport properties of growing chromia scales are important, even in the short-term. The scaling rate for chromia growth on Ni-25Cr was five times higher in Ar- $\text{H}_2$ - $\text{H}_2\text{O}$  than in Ar- $\text{O}_2$  at  $1000^\circ\text{C}$  [76]. Pure chromium oxidised two to three times faster in Ar- $\text{H}_2$ - $\text{H}_2\text{O}$  than in Ar-20% $\text{O}_2$  [75]. This effect is clearly much more important than volatilisation in these timeframes.

The importance of hydrogen doping is difficult to assess. A large amount of experimental data has been collected for reactions in air, but the importance of the low levels of  $\text{H}_2\text{O}(\text{g})$  has not been established. There is a need for comparative rate measurements for chromia growth in dry oxygen and dilute mixtures of water vapour in oxygen. As seen in Table 11.5, doubling the value of  $p_{\text{H}_2\text{O}}$  in Ar- $\text{O}_2$ - $\text{H}_2\text{O}$  gas mixtures produced only a 5% increase in rate at

**TABLE 11.6** Diffusion Controlled Chromia Scale Growth and Evaporation at  $1000^\circ\text{C}$

Alloy	Gas	$\text{kp}/\text{cm}^2\text{s}^{-1}$	Ref.	Vaporisation loss as fraction of diffusion term	
				24h	100h
Cr	$\text{O}_2$	$4 \times 10^{-14}$	56	0.1	0.15
Cr	Ar-1% $\text{O}_2$	$7 \times 10^{-12}$	55	0.007	0.01
Cr	Ar-20% $\text{O}_2$	$5 \times 10^{-12}$	75	0.008	0.02
Ni-25Cr	Ar-20% $\text{O}_2$	$7 \times 10^{-13}$	76	0.02	0.04

1000°C. However, any dopant effect might be near saturation at these levels, and a much stronger effect is found in a comparison of scaling rates at 700°C of Fe-Cr alloys in Ar-20O<sub>2</sub> and Ar-20O<sub>2</sub>-5H<sub>2</sub>O.

Measured values [91] of the parabolic rate constant for oxygen weight uptake,  $k_w$ , are listed in Table 11.7 for these gases. The duration of these experiments was restricted to 48 h in order to ensure that chromium losses due to volatilisation in the wet gas were unimportant. The scales formed were single-phase Cr<sub>2</sub>O<sub>3</sub> in all cases except for the Fe-9Cr alloy in wet gas, where breakaway oxidation produced iron-rich scales. The addition of water vapour to the gas increased chromia scaling rates by an order of magnitude for Fe-17Cr and a factor of two for Fe-25Cr.

The failure of Fe-9Cr to withstand the addition of water vapour and the success of the higher alloys can be understood simply in terms of the critical chromium concentration required to sustain continuous chromia scale growth:

$$N_{\text{Cr}}^{(0)} - N_{\text{Cr}}^i = \frac{V_{\text{FeCr}}}{V_{\text{CrO}_x}} \left( \frac{\pi k_p}{2D_{AB}} \right)^{1/2} \quad [5.22]$$

and the effect of H<sub>2</sub>O(g) on the value of  $k_p$ . Calculating  $k_p$  from the  $k_w$  value measured for Fe-17Cr in dry gas, a value of  $N_{\text{Cr}}^{(0)} - N_{\text{Cr}}^i = 0.03$  is calculated, corresponding to an interfacial value  $N_{\text{Cr}}^i = 0.07$  for the Fe-9Cr alloy (for which  $N_{\text{Cr}}^{(0)} = 0.1$ ). Thus chromia is stable for this alloy in dry gas. However, the value for  $k_w$  evidenced by Fe-17Cr in wet gas (Table 11.7) is found from [5.22] to correspond to  $N_{\text{Cr}}^{(0)} - N_{\text{Cr}}^i = 0.12$ . This condition cannot be met by Fe-9Cr, but is satisfied by both the 17Cr and 25Cr alloys. Thus the breakdown of the low chromium alloy in wet gas and the success of the higher chromium alloys is accounted for by the acceleration in chromia scaling rates. Water vapour increases the critical chromium concentration required for alloy passivation.

## 11.5 WATER VAPOUR EFFECTS ON ALUMINA GROWTH

Water vapour has been shown by Norby and Kofstad [92,93] to affect the electrical conductivity of Al<sub>2</sub>O<sub>3</sub> containing magnesium impurities. However, detailed observations of gas compositional effects on alumina scaling have not yet provided a coherent picture of the mechanisms involved.

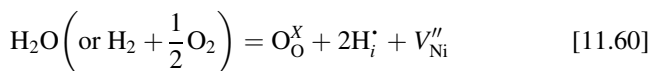
In the case of alloys, which are marginal with respect to selective alumina formation, water vapour can make a big difference. As seen in Section 6.14, water vapour promotes internal oxidation in some cases, increasing the critical alloy concentration of scale-forming metal required to achieve passivation. It can also favour the growth of nonprotective oxide scales. Boggs [94] compared the oxidation of binary Fe-Al alloys in O<sub>2</sub> and O<sub>2</sub> + H<sub>2</sub>O at 450–900°C. Scale growth was more rapid in the wet gas, because iron-rich oxide formation was favoured. Hayashi and Narita [95] compared the oxidation of Fe-5Al in

$\text{N}_2\text{-}12.2\text{H}_2\text{O}$ ,  $\text{O}_2\text{-}12.2\text{H}_2\text{O}$  and  $\text{N}_2\text{-}0.9\text{O}_2\text{-}12.2\text{H}_2\text{O}$  at  $800^\circ\text{C}$ . Internal aluminium-rich oxide precipitated, and multiple external scale layers developed in all gases. However, the reaction was very slow in  $\text{O}_2\text{-}12.2\text{H}_2\text{O}$  as a result of  $\text{FeAl}_2\text{O}_4$  developing as a single-phase layer. In  $\text{N}_2\text{-}12.2\text{H}_2\text{O}$ , faster but parabolic kinetics accompanied spinel formation as part of a two-phase  $\text{FeAl}_2\text{O}_4 + \text{FeO}$  layer. In  $\text{N}_2\text{-}0.9\text{O}_2\text{-}12.2\text{H}_2\text{O}$ , much faster scale growth reflected the development of a porous iron-rich oxide over an  $\text{FeAl}_2\text{O}_4 + \text{FeO}$  layer. Interestingly, changing the gas part way through an experiment brought about an instantaneous change in rate, indicating that the interior scale structure was accessible to the newly introduced gas.

It seems likely that these results can be explained in part using a competitive adsorption model, as was constructed for Fe-Cr in Section 11.4. Thus a high value of  $p_{\text{O}_2}$  was sufficient to prevent scale degradation by  $\text{H}_2\text{O}(\text{g})$ , but a small value was not. The new finding is that water vapour in the absence of  $\text{O}_2$  produced a slower oxidation rate than  $\text{H}_2\text{O}(\text{g})$  plus dilute oxygen. More information is required before these results can be fully understood.

Water vapour can affect the oxidation of alumina-forming alloys in two separate ways: by modifying the rate at which metastable alumina transforms to  $\alpha\text{-Al}_2\text{O}_3$  (see Section 5.10.1) and by altering the behaviour of the stable  $\alpha$ -phase. From the information available, it appears that these effects vary with both alloy type and temperature.

In the case of the alumina former, Kanthal A1 (Fe-21.5Cr-5.6Al), Buscail et al. [54] compared reactions with dry oxygen,  $\text{O}_2\text{-}15\text{H}_2\text{O}$  and  $\text{O}_2\text{-}32\text{H}_2\text{O}$  at  $1000^\circ\text{C}$ . The presence of water vapour altered the rate at which transient alumina was converted to  $\alpha\text{-Al}_2\text{O}_3$  but had negligible effect on the steady-state rate of  $\alpha\text{-Al}_2\text{O}_3$  scale growth. Similar findings were reported by Kvernes et al. [31] for the alumina former, Fe-13Cr-4.4Al at  $980^\circ\text{C}$ , and by Chevalier et al. [96] for  $\text{Fe}_3\text{Al}$  at  $950^\circ\text{C}$ . Maris-Sada et al. [97] showed that the addition of water vapour (0.1–0.5 atm) to air accelerated the growth of the transient oxide mixture formed on PWA 1484 (Ni-5.6Al-6Cr-8.7Ta-10Co-2Mo-6W-3Re,Hf) at  $1100^\circ\text{C}$ . Similar effects were reported for the model alloy Ni-8Cr-6Al. These changes were attributed to more rapid growth of NiO as a result of hydrogen doping



based on the earlier suggestion by Galerie et al. [52].

Other investigators have reported increased alumina growth rates in the presence of water vapour. Thus Leyens et al. [98] found that MCrAlY coatings oxidised up to 25% faster in  $\text{H}_2/\text{H}_2\text{O}$  than in dry air at  $1100^\circ\text{C}$ . Regina et al. [99] observed that water vapour accelerated the corrosion of FeCrAl alloys at  $500^\circ\text{C}$ . A strong temperature effect was reported by Naumenko et al. [100,101]. At temperatures of  $800\text{--}950^\circ\text{C}$ , they found that formation of fast-growing metastable alumina was promoted in  $\text{H}_2/\text{H}_2\text{O}$ , but at  $1200\text{--}1300^\circ\text{C}$ ,  $\alpha\text{-Al}_2\text{O}_3$  scales grew faster in Ar-20 $\text{O}_2$  than in Ar- $\text{H}_2\text{-H}_2\text{O}$ .



As is discussed in Chapter 13, water vapour can have a much more destructive effect on alumina scales by promoting their spallation.

## 11.6 IRON OXIDE SCALING

Although iron oxide scales are nonprotective, their growth is nonetheless a matter of practical interest. Their formation during the hot processing of steel represents material loss, and therefore a decrease in process efficiency. The need to remove these scales represents an additional cost. The consequences of incomplete scale removal for downstream processes such as rolling or coating can represent much larger economic losses, and mitigation of their initial formation is highly desirable.

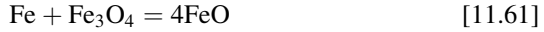
A more fundamental interest arises from the fact that high-temperature iron oxide scaling is dominated by the growth of coarse-grained wüstite,  $\text{Fe}_{1-\delta}\text{O}$ , in which mass transport is provided by lattice diffusion of metal. Indeed, wüstite scaling provided an early demonstration of the applicability of Wagner's lattice diffusion model for scaling (Section 3.7.3). However, the Wagner model predicts that for a given oxygen partial pressure, the presence or absence of water vapour has no effect on the scaling rate, and modifications to the model are clearly necessary.

Recent investigations [102–105] of the oxidation behaviour of pure iron and a low carbon, low silicon steel (0.055C-0.005Si-0.04Al-0.017Ni-0.21Mn) in  $\text{N}_2\text{-H}_2\text{-H}_2\text{O}$  reveal distinct differences between iron and steel, as seen in Fig. 11.26. Weight uptake kinetics for both metals were initially linear, changing to parabolic with time as diffusion slowed and became rate-controlling. Iron generally reacted faster than steel, but eventually developed parabolic kinetics. The effect of  $p_{\text{O}_2}$  at fixed  $p_{\text{H}_2\text{O}}$  on  $k_w$  for iron and steel is seen to be functionally similar. However, whereas the oxidation rate of steel is strongly dependent on  $p_{\text{H}_2\text{O}}$ , that of iron is not. The Arrhenius plot in Fig. 11.26D shows that activation energies for the two materials are rather similar at  $157 \text{ kJ mol}^{-1}$  for temperatures of  $800\text{--}1100^\circ\text{C}$ , but iron oxidises almost three orders of magnitude faster than steel. However, at  $1200^\circ\text{C}$ , oxidation rates are closely similar.

Both iron and steel formed single-phase wüstite scales, in accord with thermodynamic prediction for the  $\text{H}_2/\text{H}_2\text{O}$  ratios employed. In each case, the scale consisted of coarse columnar oxide grains (Fig. 11.27A). Wüstite on iron grew with a strongly preferred (100) orientation at all temperatures examined, but on steel it developed a (220) orientation from  $800$  to  $1100^\circ\text{C}$ , and a (100) orientation at  $1200^\circ\text{C}$ . Average oxide grain sizes increased with exposure time, more rapidly for iron than for steel. Grain growth rates increased with  $p_{\text{O}_2}$  at fixed  $p_{\text{H}_2\text{O}}$ , and with  $p_{\text{H}_2\text{O}}$  at constant  $p_{\text{O}_2}$ .

The slow oxidation rate of the steel in  $\text{H}_2/\text{H}_2\text{O}$  requires explanation. Since the same flowing gases supported much faster oxidation of iron, it must be concluded that the difference is due to the nature of the steel and its effect on

the product wüstite. Steel oxidation has frequently been reported (eg, [65,106]) to be slower than that of iron in the same gas. However, the usual explanations of slowed iron diffusion caused by partial scale separation or void formation, due to incorporation of alloy impurities, are inapplicable in the  $H_2/H_2O$  gases considered here, as the steel forms dense, tightly adherent scales [103,104]. Scales grown in oxygen-rich atmospheres form outer layers of  $Fe_3O_4$  and  $Fe_2O_3$ , as shown in Fig. 11.27B. Here the interfacial conversion reaction



causes a volume expansion of 13%. Some of the resulting deformation is apparent in the formation of cavities within the scale interior, a phenomenon absent in single-phase wüstite scales grown in  $H_2/H_2O$ , where the volume expansion accompanying new oxide formation is accommodated at the unconstrained external surface. Thus the slower growth of these scales on steel cannot be accounted for on the basis of macroscopic defect formation.

Lattice defect species in wüstite are mainly cation vacancies:



Taking the anion concentration as constant, and assuming the charge balance  $[V'_{Fe}] = [h^\cdot]$ , then at equilibrium

$$[V_{Fe}^\times] = K_{62}p_{O_2}^{1/2} \quad [11.64]$$

$$[V'_{Fe}] = K_{62}K_{63}^{1/2}p_{O_2}^{1/4} \quad [11.65]$$

For diffusion-controlled wüstite scaling

$$dX/dT = V_{Fe}J_{Fe} + V_OJ_O \quad [11.66]$$

where the  $V_i$  denote the volumes of oxide formed per unit flux of the indicated species. For pure wüstite,  $J_O \approx 0$ , and for diffusion of neutral iron vacancies

$$J_{Fe} = -J_V = C_V D_V \frac{d \ln a_O}{dx} \quad [3.53]$$

The predictions of this model are seen in Fig. 11.26B to succeed for iron in both the magnitude of  $k_w$  and its dependence on  $p_{O_2}$ . The same relationship between  $k_w$  and  $p_{O_2}$  applies for steel, but the oxidation rates are much slower. The simplest explanation is that the presence of impurities, such as manganese, decreases the magnitude of  $K_{62}$  and/or  $K_{63}$ , leading to decreases in vacancy concentrations, whilst preserving their  $p_{O_2}$  dependence.

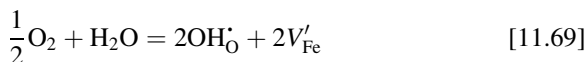
Any manganese or silicon present in the scale is too dilute to be detected by EDS, a technique with a sensitivity of about 0.1 wt%. Experimental values of  $k_w$  for steel are between 100 and 1000 times slower than for iron. It seems

unlikely that very dilute impurities in such a highly defective oxide as wüstite could yield such a large effect. Of course, it is possible that some synergistic effect between a hydrogen species derived from water vapour and an impurity from the steel is involved. No information on any such effect is available.

Steel oxidation rates in  $N_2$ - $H_2$ - $H_2O$  increase with  $p_{O_2}$  at fixed  $p_{H_2O}$  and with  $p_{H_2O}$  at fixed  $p_{H_2O}$ . An empirical relationship

$$k_w = Ap_{O_2}^{1/4} + Bp_{H_2O}^{1/2} \quad [11.67]$$

with  $A$  and  $B$  constants was established [104], suggesting two parallel reaction paths. Inert marker experiments indicated significant oxygen transport but majority metal transport supporting wüstite scale growth. These observations led to a description of solid-gas equilibrium in terms of reaction [11.64] and



If oxygen and iron transport rates are proportional to  $[OH_O^\bullet]$  and  $[V'_{Fe}]$ , the form of [11.67] can be explained.

The charge balance among the various defects in wüstite can be expressed as

$$[OH_O^\bullet] + [h^\bullet] = [H'_{Fe}] + [V'_{Fe}] \quad [11.70]$$

In the case of wüstite grown on iron,  $K_{62}$  and  $K_{63}$  are large, [11.70] is then approximated as

$$[h^\bullet] \approx [V'_{Fe}] \quad [11.71]$$

and the predominant gas-solid equilibria are described by [11.64] and [11.65].

Then  $k_w$  is predicted to vary with some weighted sum of  $p_{O_2}^{1/2}$  and  $p_{O_2}^{1/4}$ , but to be insensitive to  $p_{H_2O}$ , in agreement with the results shown in Fig. 11.26. In wüstite grown on steel,  $K_{62}$  and  $K_{63}$  are small, the charge balance is approximated as

$$[OH_O^\bullet] \approx [H'_{Fe}] \quad [11.72]$$

and the equilibrium expressions for [11.68] and [11.69] become

$$[OH_O^\bullet] \approx K_{62}^{1/2} p_{H_2O}^{1/2} \quad [11.73]$$

$$[V'_{Fe}] \approx \left( \frac{K_{63}}{K_{62}} \right)^{1/2} p_{O_2}^{1/4} \quad [11.74]$$

If wüstite scaling on steel is supported by the diffusion of iron via neutral and singly charged vacancies, and oxygen via hydroxyls, then the form of [11.67] is accounted for.

In  $O_2/H_2O$  gases, both iron and the steel grow scales of  $FeO/Fe_3O_4/Fe_2O_3$  according to parabolic kinetics at similar rates, which are reasonably close to those predicted by Wagner's theory [105]. The question then is why steel oxidises at essentially the same rate as iron in  $O_2/H_2O$ , but in  $H_2/H_2O$  the scaling of steel is much slower. Since wüstite makes up about 95% of the scale grown in  $O_2/H_2O$  and constitutes its entirety in  $H_2/H_2O$ , the properties of this layer and its boundary conditions determine oxidation rates. Dissolution of steel impurities in the oxide is expected to be similar in both cases, as are oxygen activities at the wüstite-steel boundary. Taking the example of a reaction at  $1000^\circ C$  in  $15H_2/15H_2O$ , the equilibrium value of  $p_{O_2} = 3.4 \times 10^{-15}$  atm and the  $FeO/Fe_3O_4$  boundary formed in scales grown in oxygen-rich gas has an equilibrium value of  $p_{O_2} = 2.52 \times 10^{-13}$  atm. The higher oxygen activity in the multilayer scale would be predicted from classical theory (Eq. [3.53]) to increase  $k_w$  by a factor of about 6. In actual fact,  $k_w$  increased by a factor of about 850. If, as proposed, slower wüstite growth on steel in  $H_2/H_2O$  is due to an interaction between hydrogen and an impurity, then that interaction cannot occur in wüstite grown in  $O_2/H_2O$ .

The simultaneous growth of  $Fe_3O_4$  and  $Fe_2O_3$  layers along with the wüstite in oxygen-rich gas could explain this. As seen in Section 11.4.2, the higher oxides adsorb and take up water vapour preferentially. Thus the value of  $p_{H_2O}$  in contact with wüstite will be lower in this case, and its interaction with the inner layer thereby decreased.

Current understanding of water vapour effects on wüstite scaling on steel is unsatisfactory. The observed change in oxide texture with temperature and the accompanying change in activation energy cannot be explained in terms of simple lattice defects. Whilst defect clusters with presumed crystallographic orientation preferences might account for the observations [105], no experimental evidence is available to support such a hypothesis.

## 11.7 VOID DEVELOPMENT IN GROWING SCALES

It is clear that the presence of water vapour promotes the development of voids within iron oxide scales and the iron-rich oxides formed on dilute Fe-Cr and Fe-Al alloys. Analysis of mass transport mechanisms (Section 11.4) showed that  $H_2O$  or  $H_2$  could reach these voids, and that gas-phase mass transfer within them would be rapid compared to overall scaling rates. The remaining question is to the reason these voids develop so much more readily when water vapour is present.

Void nucleation is generally thought to be due to vacancy condensation, either at the scale-metal interface [75] or within the scale [3]. Of course, such an event is impossible if the usual assumption of Wagner's model, that the flux is constant or divergence-free, applies. Recognising that pore formation corresponds to a divergence in the flux, Maruyama et al. [107,108] have calculated elemental fluxes in the magnetite scales grown on pure iron in

Ar-H<sub>2</sub>-H<sub>2</sub>O mixtures at 550°C. Applying the continuity condition to the magnetite concentration,  $C_{\text{Fe}_3\text{O}_4}$ , in the scale, they obtained

$$\frac{\partial C_{\text{Fe}_3\text{O}_4}}{\partial t} = -\frac{1}{3} \frac{\partial J_{\text{Fe}}}{\partial x} = -\frac{1}{4} \frac{\partial J_{\text{O}}}{\partial x} \quad [11.75]$$

showing explicitly that a large oxygen diffusion contribution is required for a pore to form. The effective oxygen diffusion coefficient necessary to meet this requirement was found to exceed the measured [109,110] value for  $D_{\text{O}}$  in Fe<sub>3</sub>O<sub>4</sub> by four to five orders of magnitude (Fig. 11.24). However, if oxygen transport is effected by grain boundary migration and the operation of the H<sub>2</sub>/H<sub>2</sub>O couple within the voids (Fig. 11.15), the discrepancy is accounted for.

For a void to form within an oxide, both metal and oxygen must be transported. In the case of both FeO and Fe<sub>3</sub>O<sub>4</sub> grown in dry atmospheres, oxygen anions lack mobility, and diffusion supported void growth is impossible. When hydrogen or water vapour can access the scale interior, however, oxygen mobility is effectively enhanced and voids grow.

Direct measurement of the amount of gas contained within an iron oxide scale has been attempted by Anghel et al. [111]. Iron was oxidised at 900°C, cooled and exposed to air at room temperature for 100 h. The sample was then then outgassed in a high vacuum chamber to which a mass spectrometer was attached. Analysis of the gas released from the scale showed the  $p_{\text{H}_2\text{O}}/p_{\text{N}_2}$  ratio to be 9:1, confirming the preferential uptake of water vapour. The total amount of gas released from the oxide was estimated as  $10^{-4} \text{ mol cm}^{-3}$ .

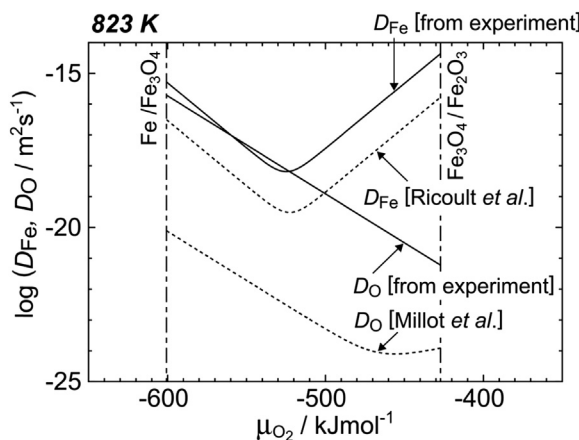
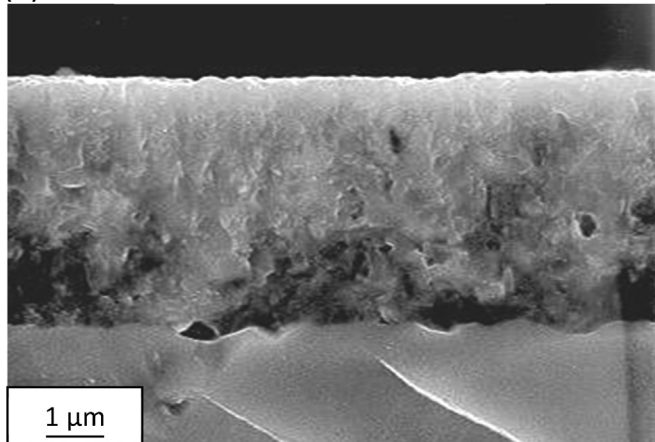


**FIGURE 11.24** Effective diffusion coefficients of iron and oxygen deduced from scale growth and pore development, compared with diffusion measurements. Published with permission from M. Ueda, K. Kawamusa, T. Maruyama, *Mater. Sci. Forum* 522–523 (2006) 37, Trans Tech Publications Ltd.

(A)



(B)

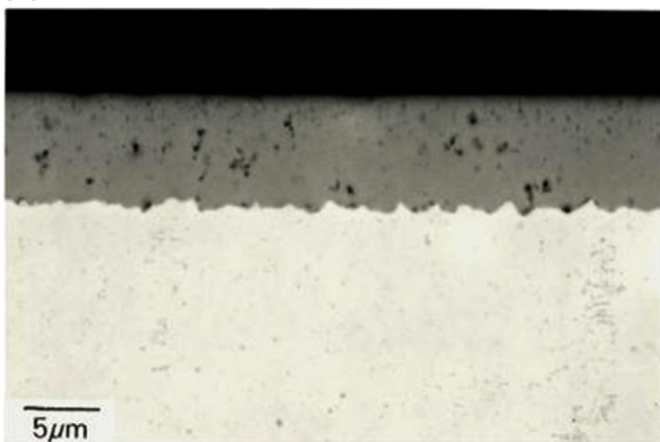
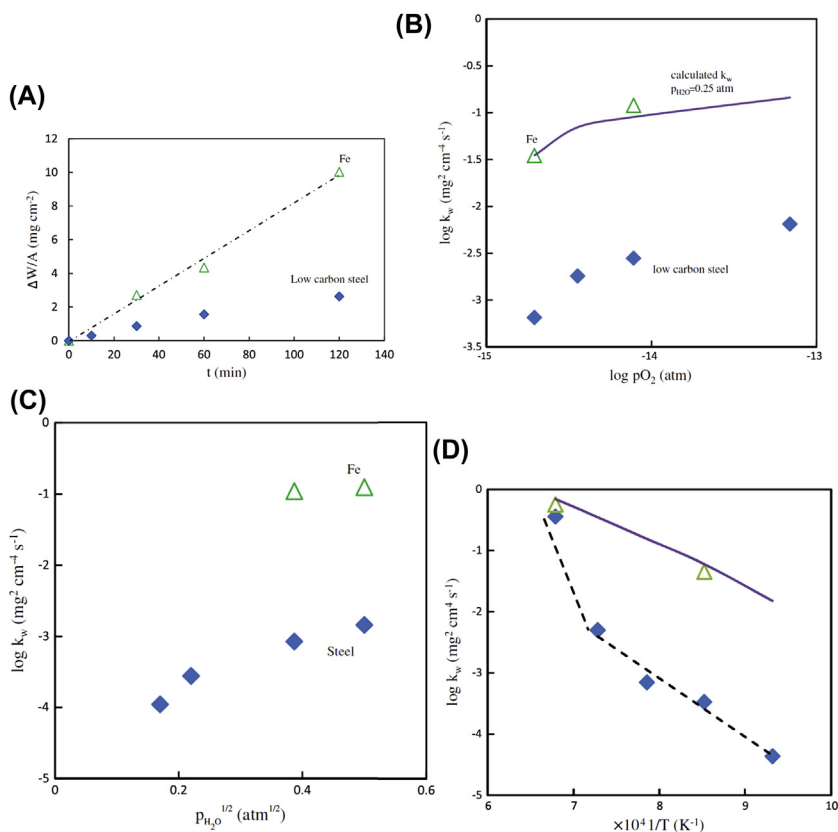


FIGURE 11.25 Chromia scales (A) grown in Ar-H<sub>2</sub>O at 900°C (*Courtesy of A. Galerie*) and (B) in N<sub>2</sub>-H<sub>2</sub>-H<sub>2</sub>O at 900°C.

However, the technique suffers from the disadvantage that damage to the oxide can be induced during cooling from reaction temperature.

Pore development in Cr<sub>2</sub>O<sub>3</sub> scales is qualitatively similar. As seen in Fig. 3.1, scales grown in O<sub>2</sub> showed very little porosity, but scales grown in Ar-H<sub>2</sub>O and in H<sub>2</sub>/H<sub>2</sub>O developed pores (Fig. 11.25). Pore volume fractions observed in Cr<sub>2</sub>O<sub>3</sub> are much smaller than those seen in iron-rich oxide scales (Fig. 11.1B). Although the presence of water vapour increases the extent of inward oxygen transport in both scales, fluxes in chromia are much smaller than in the iron oxides. Any divergences in the chromia fluxes are therefore also smaller, and the rate of pore development is seen from Eq. [11.75] to be



**FIGURE 11.26** Oxidation kinetics of iron and low carbon steel in N<sub>2</sub>-H<sub>2</sub>-H<sub>2</sub>O gases: (A) in N<sub>2</sub>-15H<sub>2</sub>-15H<sub>2</sub>O at 900°C; (B) comparison of  $p_{O_2}$  effects at fixed  $p_{H_2O} = 0.25$  atm,  $T = 985^\circ\text{C}$ ; (C) dependence on  $p_{H_2O}$  at fixed  $p_{O_2} = 3.4 \times 10^{-15}$  atm,  $T = 1000^\circ\text{C}$ ; (D) Arrhenius plot for kinetics in N<sub>2</sub>-1H<sub>2</sub>-5H<sub>2</sub>O. Continuous lines in (B) and (D) calculated from Wagner's equation for pure iron. With kind permission from D.J. Young, H. Yin, *Oxid. Met.* 79 (2013) 445, Springer Science and Business Media.

consequently slower. Apparently different porosities formed in Ar-H<sub>2</sub>O and N<sub>2</sub>-H<sub>2</sub>-H<sub>2</sub>O are interesting. However, the experiments are not directly comparable because of the different oxygen activities (and chromium defect concentrations) and the observed [112] interactions between N<sub>2</sub> and H<sub>2</sub>O transport through Cr<sub>2</sub>O<sub>3</sub>.

Little is known about pore development in alumina scales grown under isothermal conditions. The formation of cavities at the scale-alloy interface during oxidation of  $\beta$ -NiAl (Section 5.8) is thought to be governed by the diffusion properties of the alloy and its impurity content. Information on any effects water vapour might have on this process is lacking.

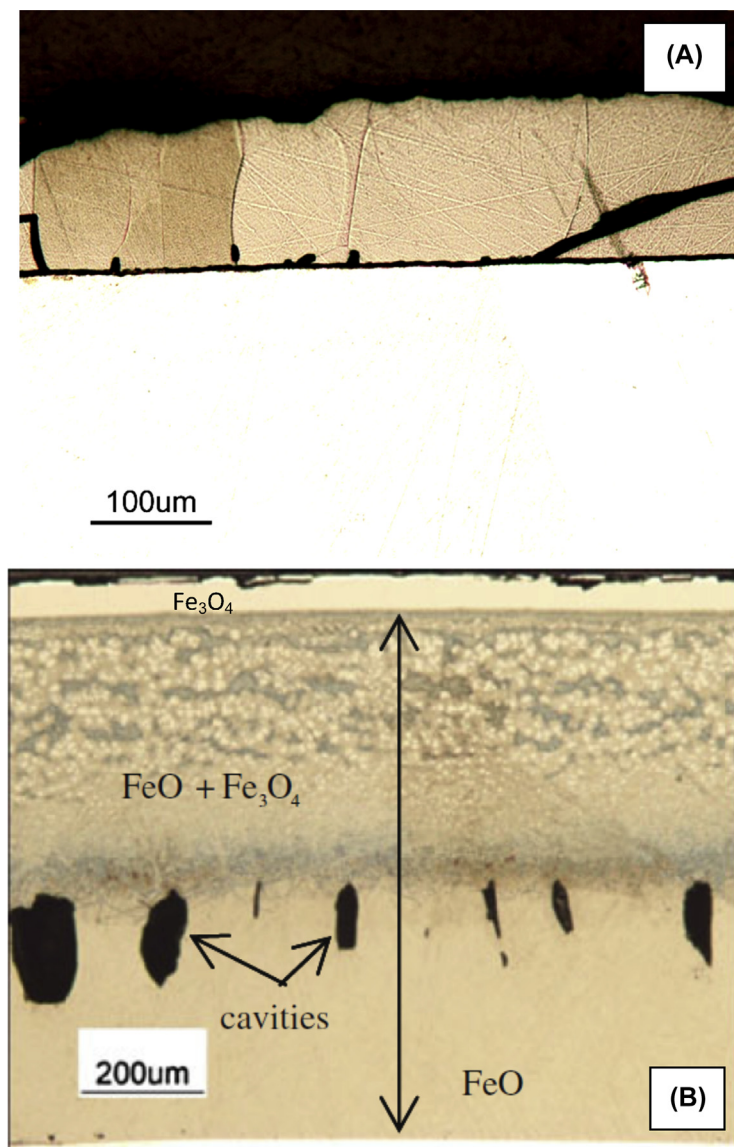


**FIGURE 11.27** Cross-sections of scales grown on iron: (A) in  $\text{N}_2\text{-15H}_2\text{-15H}_2\text{O}$  at  $985^\circ\text{C}$ ; (B) in  $\text{N}_2\text{-4O}_2\text{-6H}_2\text{O}$  at  $1200^\circ\text{C}$ . With kind permission from D.J. Young, H. Yin, *Oxid. Met.* 79 (2013) 445, Springer Science and Business Media.



## 11.8 UNDERSTANDING AND CONTROLLING WATER VAPOUR EFFECTS

At the beginning of this chapter, we noted that the problem of water vapour accelerated corrosion, and its mysterious nature had been pointed out decades ago. It is therefore reasonable to ask what progress has been made in developing a useful understanding of the processes involved. In brief, our ability to define acceptable limits to exposure conditions for particular oxides has improved greatly, and our knowledge of oxide-water vapour interaction mechanisms has expanded. However, our description of the effects is still largely qualitative, and provides guidelines rather than quantitative tools for alloy design.

Water vapour has a unique ability to accelerate volatilisation of the important oxides  $\text{Cr}_2\text{O}_3$  and  $\text{SiO}_2$ , thereby shortening the lifetimes of materials which rely on protective scales of these oxides. Fortunately, good quality thermodynamic data have become available for these reactions. As seen in [Section 11.2](#), these data can be combined with gaseous mass transfer calculations to provide accurate predictions of oxide loss rates as a function of ambient conditions. It is therefore possible to define regimes of temperature, total pressure, water vapour partial pressure and gas flow rate appropriate to desired loss rate limits. In principle, these rates can be combined with a diffusion calculation to predict depletion rates within an alloy component, and thereby arrive at lifetime estimates. Thus the present state of knowledge with regard to water vapour-driven volatilisation is satisfactory.

Our understanding of water vapour effects involved in the development of porosity in iron-rich oxide scales has improved in that the requirement of divergence in both metal and oxygen fluxes in the scale has been recognized. This requirement can only be met when the magnitude of the oxygen flux itself is much larger than can be supplied by relatively immobile lattice oxygen anions. As shown by isotope and other marker experiments, the required oxygen flux is generated when sufficient water vapour is present in the gas. The oxygen transport process involves simultaneous inwards transport of hydrogen, thereby explaining also how  $\text{H}_2\text{O}(\text{g})$  can be formed (and provide a gas-phase mass transport mechanism) within closed voids inside the scale. It is clear that this undesirable outcome can be prevented only by excluding water vapour and its derivative species from the scale interior.

A model of competitive oxygen and water vapour adsorption appears to be in qualitative agreement with the observed behaviour of iron-rich scales. It predicts that maintaining a sufficiently high  $p_{\text{O}_2}/p_{\text{H}_2\text{O}}$  ratio will prevent water vapour uptake. However, more information on just how the critical ratio depends on oxide chemistry, temperature and time is required.

Chromia scales are more resistant to pore development in wet gases, as can be understood from the low fluxes and consequently low flux divergences in

this oxide. The relatively small scale growth acceleration induced by water vapour does not support extensive pore growth. In this sense, alloying with chromium provides the same benefit in resisting both water vapour corrosion and dry oxidation. However, chromia is not completely resistant to water vapour-induced pore development.

The effects of water vapour on chromia scales are very similar to those of a reactive element metal (Section 7.5). Both segregate to oxide grain boundaries, where they have the effects of increasing oxygen transport relative to that of chromium and of refining the oxide grain structure. Both appear to improve scale-alloy adhesion. A further similarity exists at this stage: detailed information at a lattice species level is lacking for both water vapour and reactive element effects. It is to be noted that this has not prevented the exploitation of reactive element effects in alloy design.

Much less information is available for the effects of water vapour on alumina scale performance, where the situation is complicated by interactions between water vapour and transient alumina phases.

The differences between iron and carbon steel in their responses to water vapour have been clarified, but current understanding is incomplete. The behaviour of wüstite scales appears to be controlled by interactions between impurities from the steel and water vapour-derived species. It seems likely that defect clustering in the highly defective lattice is important, but evidence is lacking.

Finally, we have seen that water vapour often promotes the development of pores and voids in oxide scales. These defects obviously affect the mechanical integrity of the scale-alloy system, making scale exfoliation or spallation more likely. This problem is considered further in Chapter 13.

## REFERENCES

- [1] P. Kofstad, *High Temperature Corrosion*, Elsevier Applied Science, London, 1988.
- [2] D.L. Douglass, P. Kofstad, A. Rahmel, G.C. Wood, *Oxid. Met.* 45 (1996) 529.
- [3] S.R.J. Saunders, L.N. McCartney, *Mater. Sci. Forum* 522–523 (2006) 119.
- [4] W.J. Quadakkers, J. Zurek, in: *Shreir's Corrosion*, fourth ed., vol. 1, Elsevier, 2010, pp. 407–456.
- [5] S. Chevalier, J. Favergeon (Eds.), *French Activity on High Temperature Corrosion in Water Vapour*, Trans Tech Publications Ltd., Switzerland, 2014.
- [6] J. Ehlers, D.J. Young, E.J. Smaardijk, A.K. Tyagi, H.J. Penkalla, L. Singheiser, W.J. Quadakkers, *Corros. Sci.* 48 (2006) 3428.
- [7] O. Knacke, O. Kubaschewski, K. Hesselmann, *Thermochemical Properties of Inorganic Substances*, second ed., Springer-Verlag, Berlin, 1991.
- [8] M.W. Chase, *NIST-JANAF Thermochemical Tables*, J. Phys. Chem. Reference Data, Monograph No. 9, Institute of Physics, Woodbury, NY, 1999.
- [9] G.R. Belton, F.D. Richardson, *Trans. Faraday Soc.* 58 (1962) 1562.
- [10] E.J. Opila, D.L. Myers, N.S. Jacobson, I.M.D. Nielson, D.F. Johnson, J.K. Olminky, M.D. Allendorf, *J. Phys. Chem. A* 111 (2007) 1971.

- [11] E.J. Opila, D.L. Myers, J. Am. Ceram. Soc. 87 (2004) 1701.
- [12] A. Hashimoto, Geochim. Cosmochim. Acta 56 (1992) 511.
- [13] E.J. Opila, D.S. Fox, N.S. Jacobson, J. Am. Ceram. Soc. 80 (1997) 1009.
- [14] N. Jacobson, D. Myers, E.J. Opila, E. Copland, J. Phys. Chem. Solids 66 (2005) 471.
- [15] D. Caplan, M. Cohen, Corrosion 15 (1959) 57.
- [16] D.R. Sigler, Oxid. Met. 46 (1996) 335.
- [17] H. Nickel, Y. Wouters, M. Thiele, W.J. Quadackers, Fresenius J. Anal. Chem. 361 (1998) 540.
- [18] H. Asteman, J.-E. Svensson, M. Norell, L.-G. Johansson, Oxid. Met. 54 (2000) 11.
- [19] R. Pieraldi, B.A. Pint, Oxid. Met. 61 (2004) 463.
- [20] B.A. Pint, J.M. Rakowski, in: Corrosion 2000, NACE, Houston, TX, 2000. Paper 259.
- [21] H. Asteman, J.-E. Svensson, L.-G. Johansson, M. Norell, Oxid. Met. 52 (1999) 95.
- [22] B.B. Ebbinghaus, Combust. Flame 93 (1993) 119.
- [23] D.R. Gaskell, An Introduction to Transport Phenomena in Materials Engineering, Momentum Press, 2012.
- [24] D.J. Young, B.A. Pint, Oxid. Met. 66 (2006) 137.
- [25] B.A. Pint, J. Eng. Gas Turbines Power 128 (2006) 370.
- [26] B.A. Pint, ASME Paper # GT2005-68495, New York, 2005.
- [27] C.S. Tedmon, J. Electrochem. Soc. 113 (1966) 766.
- [28] S. Jianian, Z. Longjiang, L. Tiefan, Oxid. Met. 48 (1997) 347.
- [29] E.A. Gulbransen, T.P. Copen, Nature 186 (1960) 959.
- [30] A.S. Khanna, P. Kofstad, in: M.J. Bennett, G.W. Lorimer (Eds.), Microscopy of Oxidation, Institute of Metals, London, 1990, p. 113.
- [31] I. Kvernes, M. Oliveira, P. Kofstad, Corros. Sci. 17 (1977) 273.
- [32] R.A. Rapp, Met. Trans. A A15 (1984) 765.
- [33] J. Bailey, J. Electrochem. Soc. 144 (1997) 3568.
- [34] P. Kofstad, Solid State Ionics 52 (1992) 69.
- [35] D. Das, M. Miller, H. Nickel, K. Hilpert, in: U. Bossel (Ed.), Proceedings of 1st European Solid Oxide Fuel Cell Forum, vol. 2, 1994, p. 703.
- [36] W.J. Quadackers, H. Greiner, M. Hänsel, A. Pattanaik, A.S. Khanna, W. Mallener, Solid State Ionics 91 (1996) 55.
- [37] E.J. Opila, N.S. Jacobson, Oxid. Met. 44 (1995) 527.
- [38] T. Narushima, T. Goto, Y. Yokoyama, Y. Iguchi, T. Hirai, J. Am. Ceram. Soc. 76 (1993) 2521.
- [39] E.J. Opila, R.E. Hann, J. Am. Ceram. Soc. 80 (1997) 197.
- [40] R.C. Robinson, J.L. Smialek, J. Am. Ceram. Soc. 82 (1999) 1817.
- [41] E.J. Opila, J.L. Smialek, R.C. Robinson, D.S. Fox, N.S. Jacobson, J. Am. Ceram. Soc. 82 (1999) 1826.
- [42] J.L. Smialek, R.C. Robinson, E.J. Opila, D.S. Fox, N.S. Jacobson, Adv. Compos. Mater. 8 (1999) 33.
- [43] K.L. More, P.F. Tortorelli, M.K. Ferber, J.R. Keiser, J. Am. Ceram. Soc. 83 (2000) 211.
- [44] M.K. Ferber, H.T. Lin, V. Parthasary, R.A. Wenglarz, in: Proceedings of IGTI Conference (Munich), ASME, New York, 2000. Paper No. 2000-GT-0661.
- [45] E.J. Opila, J. Am. Ceram. Soc. 86 (2003) 1238.
- [46] M.K. Næss, D.J. Young, J. Zhang, J.E. Olsen, G. Tranell, Oxid. Met. 78 (2012) 363.
- [47] C. Wagner, J. App. Phys. 29 (1958) 1295.
- [48] E.J. Opila, N.S. Jacobson, D.L. Myers, E.H. Copland, JOM 58 (2006) 22.
- [49] D. Zhu, N.P. Bansal, R.A. Miller, NASA/TM-2003-212 544, NASA, Washington, DC, 2003.

- [50] O.H. Krikorian, *High Temp. High Pressure* 14 (1982) 387.
- [51] E.T. Turkdogan, W.M. McKewan, L. Zwell, *J. Phys. Chem.* 69 (1965) 327.
- [52] A. Galerie, Y. Wouters, M. Cailliet, *Mater. Sci. Forum* 369–372 (2001) 231.
- [53] N.N. Greenwood, *Ionic Crystals, Lattice Defects and Nonstoichiometry*, Chemical Publishing Company, New York, 1970.
- [54] H. Buscail, S. Heinze, P. Dufour, J.P. Larpin, *Oxid. Met.* 47 (1997) 445.
- [55] M. Hänsel, W.J. Quadakkers, D.J. Young, *Oxid. Met.* 59 (2003) 285.
- [56] D. Caplan, M. Cohen, *Corros. Sci.* 7 (1967) 725.
- [57] L.B. Pfeil, *J. Iron Steel Inst.* 119 (1929) 501.
- [58] A. Dravnieks, H.J. McDonald, *J. Electrochem. Soc.* 94 (1948) 139.
- [59] C.T. Fujii, R.A. Meussner, *J. Electrochem. Soc.* 110 (1963) 1195.
- [60] C.T. Fujii, R.A. Meussner, *J. Electrochem. Soc.* 111 (1964) 1215.
- [61] A. Rahmel, J. Tobolski, *Corros. Sci.* 5 (1965) 333.
- [62] A. Rahmel, *Werkst. Korros.* 16 (1965) 662.
- [63] M. Thiele, H. Teichmann, W. Schwarz, W.J. Quadakkers, *VGB KraftwerksTechnik*. 77 (1997) 135, 2/97 (1997) 129.
- [64] W.J. Quadakkers, M. Thiele, P.J. Ennis, H. Teichmann, W. Schwarz, in: *Eurocorr 97, Proceedings, European Federation of Corrosion*, vol. II, 1997, p. 35.
- [65] C.W. Tuck, M. Odgers, K. Sachs, *Werkst. Korros.* 7 (1966) 48.
- [66] C.W. Tuck, M. Odgers, K. Sachs, *Corros. Sci.* 9 (1969) 271.
- [67] B.E. Deal, A.S. Grove, *J. Appl. Phys.* 36 (1965) 3770.
- [68] A.J. Moulson, J.P. Roberts, *Trans. Faraday Soc.* 57 (1961) 1208.
- [69] M. Schutze, D. Renusch, M. Schorr, *Corros. Eng. Sci. Technol.* 39 (2004) 157.
- [70] S. Hayashi, T. Narita, *Oxid. Met.* 56 (2001) 251.
- [71] B. Tveten, G. Hultquist, D. Wallinder, *Oxid. Met.* 55 (2001) 279.
- [72] B. Tveten, G. Hultquist, T. Norby, *Oxid. Met.* 51 (1999) 221.
- [73] G. Hultquist, B. Tveten, E. Hornlund, *Oxid. Met.* 54 (2000) 1.
- [74] W.J. Quadakkers, J.F. Norton, S. Canetoli, K. Schuster, A. Gil, in: S.B. Newcomb, J.A. Little (Eds.), *Microscopy of Oxidation 3*, Institute of Metals, London, 1996, p. 221.
- [75] M. Michalik, M. Hänsel, J. Zurek, L. Singhheiser, W.J. Quadakkers, *Mater. High Temp.* 22 (2005) 213.
- [76] J. Zurek, D.J. Young, E. Essuman, M. Hänsel, H.J. Penkalla, L. Niewolak, W.J. Quadakkers, *Mater. Sci. Eng. A* 477 (2008) 259–270.
- [77] R. Francis, D.G. Lees, *Corros. Sci.* 16 (1976) 847.
- [78] D.G. Lees, J.M. Calvert, *Corros. Sci.* 16 (1976) 767.
- [79] K.P.R. Reddy, J.L. Smialek, A.R. Cooper, *Oxid. Met.* 17 (1982) 429.
- [80] O.T. Goncel, J. Stringer, D.P. Whittle, *Corros. Sci.* 18 (1978) 701.
- [81] K. Przybylski, A.J. Garratt-Reed, G.J. Yurek, *J. Electrochem. Soc.* 135 (1988) 509.
- [82] K. Przybylski, G.J. Yurek, *J. Electrochem. Soc.* 135 (1988) 517.
- [83] M. Nakai, K. Nagai, Y. Murata, M. Morinaga, S. Matsuda, M. Kanno, *ISIJ Int.* 45 (2005) 1066.
- [84] A. Yamauchi, Y. Yamauti, Y. Hirohata, T. Hino, K. Kurokawa, *Mater. Sci. Forum* 522–523 (2005) 163.
- [85] T. Norby, *Adv. Ceram.* 23 (1987) 107.
- [86] T. Norby, *J. Phys. IV* 3 (1993) 99.
- [87] D.G. Thomas, J.J. Lander, *J. Chem. Phys.* 25 (1956) 1136.
- [88] S. Stotz, C. Wagner, *Phys. Chem.* 72 (1968) 778.
- [89] D.A. Shores, R.A. Rapp, *J. Electrochem. Soc.* 119 (1972) 300.

- [90] F.A. Kröger, *The Chemistry of Imperfect Crystals*, North Holland, Amsterdam, 1974.
- [91] N.K. Othman, J. Zhang, D.J. Young, *Oxid. Met.* 73 (2010) 337.
- [92] T. Norby, in: O. Johannessen, A.G. Andersen (Eds.), *Selected Topics in High Temperature Chemistry: Defect Chemistry of Solids*, Elsevier, Amsterdam, 1989, p. 101.
- [93] T. Norby, P. Kofstad, *High Temp. High Pressures* 20 (1988) 345.
- [94] W.E. Boggs, *J. Electrochem. Soc.* 118 (1971) 6, 906.
- [95] S. Hayashi, T. Narita, *Oxid. Met.* 58 (2002) 319.
- [96] S. Chevalier, P. Juzon, K. Przybylski, J.P. Larpin, *Sci. Technol. Adv. Mater.* 10 (2009) 045006.
- [97] M.C. Maris-Sada, G.H. Meier, F.S. Pettit, *Met. Mater. Trans.* 34A (2003) 2609.
- [98] C. Leyens, K. Fritscher, R. Gehrling, M. Peters, W.A. Kaysser, *Surf. Coat. Technol.* 82 (1996) 133.
- [99] J.R. Regina, J.N. DuPont, A.R. Marder, *Oxid. Met.* 61 (2004) 69.
- [100] D. Naumenko, W.J. Quadakkers, A. Galerie, Y. Wouters, S. Jourdain, *Mater. High Temp.* 20 (2003) 287.
- [101] D.J. Young, D. Naumenko, E. Wessel, L. Singheiser, W.J. Quadakkers, *Mater. Corros.* 61 (2010) 838.
- [102] R.Y. Chen, W.Y.D. Yuen, *Oxid. Met.* 59 (2003) 433.
- [103] H. Yin, S.L.I. Chan, W.Y.D. Yuen, D.J. Young, *Oxid. Met.* 77 (2012) 305.
- [104] H. Yin, W.Y.D. Yuen, D.J. Young, *Mater. Corros.* 63 (2012) 869.
- [105] D.J. Young, H. Yin, *Oxid. Met.* 79 (2013) 445.
- [106] R.Y. Chen, W.Y.D. Yuen, *Met. Mat. Trans. A* 40A (2009) 3091.
- [107] T. Maruyama, N. Fukagai, M. Uedu, K. Kawamura, *Mater. Sci. Forum* 461–464 (2004) 807.
- [108] M. Ueda, K. Kawamura, T. Maruyama, *Mater. Sci. Forum* 522–523 (2006) 37.
- [109] F. Millot, J.C. Lorin, B. Klossa, Y. Niu, J.R. Tarento, *Ber. Bunsenges. Phys. Chem.* 101 (1997) 1351.
- [110] J.E. Castle, P.L. Surnam, *J. Phys. Chem.* 71 (1967) 4255, 73 (1969) 632.
- [111] C. Anghel, G. Hultquist, Q. Dong, J. Rundgren, I. Saeki, M. Limbäck, *Mater. Sci. Forum* 522–523 (2006) 93.
- [112] X.G. Zheng, D.J. Young, *Oxid. Met.* 42 (1994) 163.